The Astrophysical Journal, 853:177 (17pp), 2018 February 1 https://doi.org/10.3847/1538-4357/aaa54b

The Origin of Molecular Clouds in Central Galaxies

F. A. Pulido[1], B. R. McNamara[1,2], A. C. Edge[3], M. T. Hogan[1,2], A. N. Vantyghem[1], H. R. Russell[4], P. E. J. Nulsen[5,6], I. Babyk[1,7], and P. Salomé[8]
[1] Department of Physics and Astronomy, University of Waterloo, 200 University Avenue W, Waterloo, ON N2L 3G1, Canada
[2] Perimeter Institute for Theoretical Physics, 31 Caroline Street North, Waterloo, ON N2L 2Y5, Canada
[3] Department of Physics, University of Durham, South Road, Durham DH1 3LE, UK
[4] Institute of Astronomy, Madingley Road, Cambridge CB3 0HA, UK
[5] Harvard-Smithsonian Center for Astrophysics, 60 Garden Street, Cambridge, MA 02138, USA
[6] International Centre for Radio Astronomy Research (ICRAR), University of Western Australia, 35 Stirling Highway, Crawley, WA 6009, Australia
[7] Main Astronomical Observatory of NAS of Ukraine, 27 Akademika Zabolotnogo Street, 03143, Kyiv, Ukraine
[8] Observatoire de Paris, LERMA, CNRS, PSL University, Sorbonne University UPMC, Paris, France
Received 2017 October 10; revised 2017 December 19; accepted 2018 January 1; published 2018 February 5

Abstract

We present an analysis of 55 central galaxies in clusters and groups with molecular gas masses and star formation rates lying between 10^8 and 10^{11} $M_\odot$ and 0.5 and 270 $M_\odot$ yr^{-1}, respectively. Molecular gas mass is correlated with star formation rate, Hα line luminosity, and central atmospheric gas density. Molecular gas is detected only when the central cooling time or entropy index of the hot atmosphere falls below ~1 Gyr or ~35 keV cm^2, respectively, at a (resolved) radius of 10 kpc. These correlations indicate that the molecular gas condensed from hot atmospheres surrounding the central galaxies. We explore the origins of thermally unstable cooling by evaluating whether molecular gas becomes prevalent when the minimum of the cooling to free-fall time ratio ($t_{\rm cool}/t_{\rm ff}$) falls below ~10. We find that (1) molecular gas-rich systems instead lie between $10 < \min(t_{\rm cool}/t_{\rm ff}) < 25$, where $t_{\rm cool}/t_{\rm ff} = 25$ corresponds approximately to cooling time and entropy thresholds of 1 Gyr and 35 keV cm^2, respectively; (2) $\min(t_{\rm cool}/t_{\rm ff})$ is uncorrelated with molecular gas mass and jet power; and (3) the narrow range $10 < \min(t_{\rm cool}/t_{\rm ff}) < 25$ can be explained by an observational selection effect, although a real physical effect cannot be excluded. These results and the absence of isentropic cores in cluster atmospheres are in tension with models that assume thermal instability ensues from linear density perturbations in hot atmospheres when $t_{\rm cool}/t_{\rm ff} \lesssim 10$. Some of the molecular gas may instead have condensed from atmospheric gas lifted outward by buoyantly rising X-ray bubbles or by dynamically induced uplift (e.g., mergers, sloshing).

Key words: galaxies: clusters: general – galaxies: clusters: intracluster medium – galaxies: star formation

1. Introduction

Our understanding of the origin and fate of molecular gas in galaxies is central to our understanding of galaxy formation. Large galaxy surveys such as the Sloan Digital Sky Survey firmly established the bimodality in the color distribution of local galaxies representing the so-called blue cloud and red sequence (Baldry et al. 2004). The blue cloud generally consists of star-forming spiral galaxies rich in molecular gas, while the red sequence is largely composed of quiescent elliptical galaxies (Strateva et al. 2001). This bimodality appears to result from an abrupt decrease in star formation that causes a rapid transition of galaxies from the blue cloud to the red sequence. (Baldry et al. 2004; Thomas et al. 2005; Faber et al. 2007). Star-forming regions in galaxies tend to correlate with bright H_2 regions (Leroy et al. 2008). Galaxies lacking star formation are also depleted in molecular gas. Thus, understanding the origin of molecular gas is critical to our understanding of galaxy formation.

Some of the largest reservoirs of molecular gas are found in central cluster galaxies, which are the most massive elliptical-like galaxies known. These galaxies, dubbed brightest cluster galaxies (BCGs), lie at the centers of galaxy clusters and groups. Clusters and groups are embedded in hot, tenuous atmospheres whose temperatures lie between 10^{7-8} K. Their central cooling times are often less than the Hubble time. The galaxies lying at their centers are expected to accumulate molecular gas that has condensed from the atmospheres (Fabian 1994). Searches for this accumulated cool gas in clusters have covered a broad range of temperatures: soft X-ray emission (Peterson et al. 2003), ionized gas at $10^{5.5}$ K (Bregman et al. 2006), ionized gas at 10^4 K (Crawford et al. 1999), neutral gas at 10^3 K (O'Dea et al. 1998), warm molecular hydrogen gas at 1000–2500 K (Edge et al. 2002), and cold molecular hydrogen gas at 20–40 K (Edge 2001; Salomé & Combes 2003). Of these components, cold molecular hydrogen (which we refer to as molecular gas from here on), with masses lying between 10^{9-11} $M_\odot$, far outweighs the others. Early searches for molecular gas in clusters resulted in H_2 upper limits of $\sim 10^{8-10}$ $M_\odot$ (Bregman & Hogg 1988; Grabelsky & Ulmer 1990; McNamara & Jaffe 1994; O'Dea et al. 1994) and one detection in NGC 1275 centered in the Perseus cluster (Lazareff et al. 1989; Mirabel et al. 1989).

A breakthrough came with the detection of molecular gas in the central galaxies of 20 cooling clusters (Edge 2001; Salomé & Combes 2003) using IRAM 30 m and JCMT 15 m telescope observations of clusters selected from the *ROSAT* ALL-sky Survey (Crawford et al. 1999). Although the molecular gas reservoirs are large, they account for less than 10% of the mass expected from pure cooling models (Edge & Frayer 2003), indicating that cooling is suppressed. Observations have since shown that radio-mechanical feedback from the active galactic nuclei (AGN) hosted by the BCG is the most plausible heating mechanism. In response to the cooling of the ICM, the AGN launches radio jets that inflate cavities and spawn shock waves in the surrounding atmospheres. The heat dissipated in the

surrounding atmosphere via sound waves, shocks, turbulence, and cosmic rays nearly balance cooling (see reviews by McNamara & Nulsen 2007, 2012; Fabian 2012). Molecular gas is an essential element of feedback, as it potentially links the fuel powering the AGN to the atmosphere that spawned it (Pizzolato & Soker 2005; McNamara et al. 2011; Gaspari et al. 2012).

1.1. Molecular Cloud Formation by Thermally Unstable Cooling

We investigate here the origin of molecular gas in central galaxies. Molecular clouds and star formation in central galaxies have for decades been associated with short central atmospheric cooling times. High resolution X-ray observations from *Chandra* revealed a sharp threshold in cooling time: when the atmospheric cooling time in central cluster galaxies falls below ~1 Gyr, star formation and Hα emission frequently appears (Cavagnolo et al. 2008; Rafferty et al. 2008). While the cooling time threshold clearly implicates thermally unstable cooling as the origin of molecular gas and star formation (Nulsen 1986; Pizzolato & Soker 2005), the cooling time threshold lacked a cogent theoretical explanation.

Recent and potentially important developments have led some to suggest thermal instability ensues instead when the ratio of the cooling to free-fall time timescales, $t_{\rm cool}/t_{\rm ff}$, lies well above unity (McCourt et al. 2012; Gaspari et al. 2013; Li et al. 2015; Prasad et al. 2015; Singh & Sharma 2015; Voit & Donahue 2015; Prasad et al. 2017). Sharma et al. (2012) suggested that thermally unstable cooling can arise from linear perturbations when $t_{\rm cool}/t_{\rm ff} \lesssim 10$. This conjecture was tested by McCourt et al. (2012), Voit & Donahue (2015), and Li et al. (2015), who showed that central galaxies with bright nebular emission lie in the range $5 \lesssim t_{\rm cool}/t_{\rm ff} \lesssim 30$. Although most systems with signatures of cooling gas lie above 10, a significant number lying below 10 seemed to confirm this conjecture. The systems lying below 10 were presumably cooling rapidly, while those above were or are being stabilized by AGN feedback in response to an earlier cooling event.

Subsequently, Voit et al. (2015a) found fewer objects lying below 10, suggesting that $t_{\rm cool}/t_{\rm ff} \lesssim 10$ represents a floor maintained by a global balance between heating and cooling, rather than a threshold. Excursions below 10 occur infrequently, as the atmosphere is cycling through a more rapid episode of cooling. This phase presumably occurs when radio jets become inactive as the fuel levels subside. More recently, Choudhury & Sharma (2016) showed that the three-dimensional geometry of an atmosphere is in fact unimportant, undermining the theoretical justification for cold gas condensation when $t_{\rm cool}/t_{\rm ff} \lesssim 10$.

While pursuing a broader program intended to study the relationship between feedback and halo mass (Main et al. 2017), McNamara et al. (2016) and Hogan et al. (2017a, 2017b) analyzed a large data set of clusters, paying careful attention to modeling resolution effects and the gravitational potential of the central galaxy. Statistical tests were performed to determine whether $t_{\rm cool}/t_{\rm ff}$ is influenced primarily by the numerator or denominator, a test ignored in earlier studies. If $t_{\rm cool}/t_{\rm ff}$ were indeed the thermodynamic parameter driving thermally unstable cooling, the scatter in the correlations between Hα emission, star formation, molecular gas, and atmospheric cooling time should decline (e.g., McCourt et al. 2012). It does not. McNamara et al. (2016), Hogan et al. (2017b), and we here show that in cluster atmospheres, $t_{\rm cool}/t_{\rm ff}$ is governed statistically almost entirely by the cooling time and not the free-fall time. While cooling times span more than a decade, the radial free-fall time profiles show a much narrower spread (Hogan et al. 2017b). At 10 kpc they vary by less than a factor of two.

We confirm here and in Hogan et al. (2017b) the floor at $t_{\rm cool}/t_{\rm ff} \sim 10$ found by (Voit et al. 2015a). Extending this analysis to nearly 100 systems, we find no evidence of significant departures below 10, as reported by Voit & Donahue (2015), McCourt et al. (2012), and Li et al. (2015). While our analysis does not exclude a role for $t_{\rm cool}/t_{\rm ff}$ in thermally unstable cooling, its role is not obvious. This is problematic for thermally unstable cooling models that assume thermal instability arises from small, linear density perturbations. Nevertheless, the floor reported by Voit et al. (2015a) is a potentially important development that needs to be understood.

Panagoulia et al. (2014), Hogan et al. (2017b), and this work have shown that resolution is a crucial factor in the inner few arcsec, and that it must be taken into account. Hogan et al. (2017b) found that the minimum in $t_{\rm cool}/t_{\rm ff}$ followed by an inward rise as the profile approaches the nucleus is almost certainly a resolution bias in most systems. Instead, the $t_{\rm cool}/t_{\rm ff}$ profile reaches a minimum and flattens to a constant with radius into the nucleus in many systems. The inner flat $t_{\rm cool}/t_{\rm ff}$ profile arises naturally in an isothermal potential when the entropy profile scales as $K \propto R^{2/3}$. This scaling was shown to be prevalent in clusters by Panagoulia et al. (2014), and has since been shown to be a general property of galactic hot atmospheres across a broad range of masses and morphological types (Hogan et al. 2017b). Observations show that systems become thermally unstable where the local value $t_{\rm cool}/t_{\rm ff}$ lies well above 10. But the most unstable region is the flat $t_{\rm cool}/t_{\rm ff}$ core.

A deeper understanding is emerging from new observations made with the Atacama Large Millimeter Array (ALMA) that have resolved the molecular clouds in more than a half dozen systems (David et al. 2014; McNamara et al. 2014; Russell et al. 2014, 2017, 2016; Vantyghem et al. 2016). In several systems, the molecular clouds lie in filamentary distributions located beneath the X-ray bubbles, indicating a direct link between molecular clouds and the AGN feedback process. Unlike spiral galaxies, the molecular clouds in BCGs rarely lie in disks or rings. These studies indicated that molecular gas is being lifted, or condensing, in the wakes of rising X-ray bubbles.

Motivated by these observations and the uplift model of Revaz et al. (2008), in McNamara et al. (2014, 2016), we proposed an alternative model where low entropy gas becomes thermally unstable when it is lifted to an altitude where its cooling time is much shorter than its infall time, $t_{\rm cool}/t_{\rm I} \lesssim 1$. Here the infall timescale, $t_{\rm I}$, is determined by the slower of the free-fall speeds and the terminal speed of the thermally unstable. Our conjecture closely follows the pioneering work of Pizzolato & Soker (2005). The significance of uplift has been recognized and is now an integral aspect of precipitation (Voit et al. 2017a) and chaotic cold accretion (Gaspari et al. 2012). However, we have dubbed our mechanism "stimulated feedback," to be clear. Our measurements do not reveal a clear role the free-fall time plays in thermally unstable cooling as it applies to the radially averaged thermodynamic properties of hot atmospheres. Based on the growing body of ALMA

Table 1
IRAM and ALMA Molecular Gas

System	Transition	IRAM ($10^8\ M_\odot$)	ALMA ($10^8\ M_\odot$)
2A0335+096	CO(1−0)	17 ± 5	11.3 ± 1.5
A1664	CO(1−0)	280 ± 90	110 ± 10
A1835	CO(1−0)	650 ± 210	490 ± 20
A2597	CO(1−0)	26 ± 13	⋯
	CO(2−1)	14 ± 5	18 ± 2
NGC 5044	CO(1−0)	2.3 ± 0.8	⋯
	CO(2−1)	0.61 ± 0.2	0.51
PKS 0745−191	CO(1−0)	40 ± 9	46 ± 9
Phoenix	CO(3−2)	⋯	210 ± 40

Note. Molecular gas mass derived from IRAM observations shown above was calculated using data from A. C. Edge (2018, in preparation). References for ALMA observations include 2A0335+096-Vantyghem et al. (2016), A1664-Russell et al. (2014), A1835-McNamara et al. (2014), A2597-Tremblay et al. (2016), NGC 5044-David et al. (2014), PKS 0745−191-Russell et al. (2016), and Phoenix-Russell et al. (2017). An alternative name for 2A0335+096 is RXC J0338.6+0958.

observations, a link between molecular clouds and uplifted gas implicates uplift as an important mechanism. This process can then be directly linked to the cannonical $t_{\rm cool}/t_{\rm I} \lesssim 1$ by increasing the free-fall time. The puzzling discovery that molecular clouds move well below the free-fall speed (McNamara et al. 2014; Russell et al. 2014, 2017, 2016) motivated us to suggest that the infall timescale may be longer than the free-fall timescale (limited by the terminal speed) would enhance thermally unstable cooling, even in regions where $t_{\rm cool}/t_{\rm I} \gg 1$.

We present an analysis of 55 giant elliptical galaxies situated in the cores of clusters and groups, from which 33 are detected with molecular gas. Section 2 describes the sample consisting of systems observed with the IRAM 30 m telescope. Section 3 describes the analyses taken to derive the molecular gas mass, ICM properties from *Chandra* X-ray data, and cluster mass profiles following the procedure of Hogan et al. (2017a). Sections 4 and 5 present the results of these analyses and discussions regarding the connection of molecular gas with properties of the ICM and AGN.

Throughout this paper, we have assumed a standard ΛCDM cosmology with $\Omega_{\rm m} = 0.3$, $\Omega_\Lambda = 0.7$, and $\rm H_0 = 70\ km\ s^{-1}\ Mpc^{-1}$.

2. Data Sample

Our sample is composed of 55 central dominant galaxies drawn from the CO surveys of Edge (2001), Salomé & Combes (2003), and others observed since these publications with the IRAM 30 m by A. C. Edge (2018, in preparation). The sample was selected by a combination of properties, including substantial mass cooling rate and nebular emission (Crawford et al. 1999). The correlation between molecular gas mass and Hα luminosity was previously found by Edge (2001) and Salomé & Combes (2003), and is apparent in our sample, as shown in Figure 1. We complement these earlier CO studies with X-ray data drawn from the *Chandra* Data Archive by deriving mass profiles and other thermodynamic properties. The molecular gas masses of objects in our IRAM sample is compared with that of ALMA observations as shown in Table 1. Coordinates and X-ray observation properties for our sample are summarized in Tables 2 and 3, respectively. Our

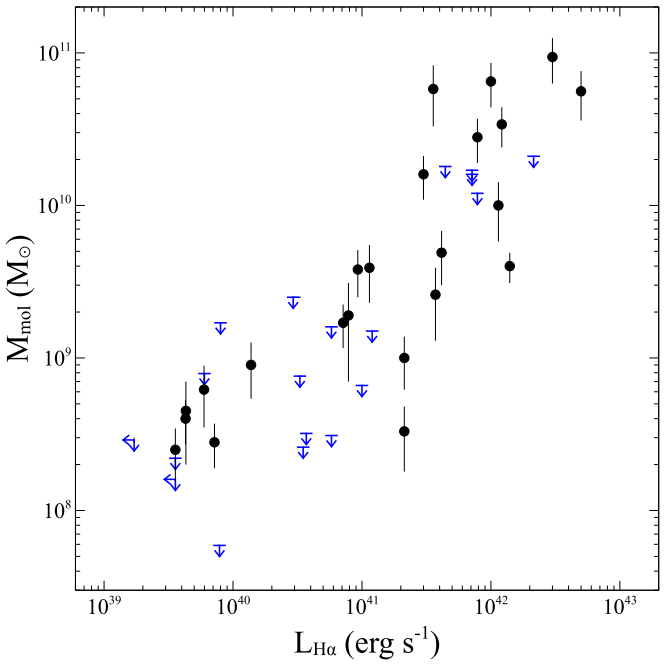

Figure 1. Molecular gas mass vs. Hα luminosity for our sample. Black symbols denote systems observed with CO emission, while blue symbols denote upper limits.

sample includes 33 systems detected in CO with derived molecular gas masses in the range $\sim 10^{8-11}\ M_\odot$, and 22 systems with CO upper limits. Because our sample is not complete in a volume or flux limited sense, we avoid discussion of issues that may be affected by this bias. Nevertheless, the sample represents the properties of systems over a 4 decade range of nebular luminosity and a 3 decade range of molecular gas mass (Figure 1).

3. Analysis

We investigate the plausibility that molecular gas is condensing from hot atmospheres and is fueling star formation and AGN activity in central galaxies. We explore the properties of the surrounding hot atmospheres and their relationship to the molecular gas observed in central galaxies. Section 3.1 discusses the molecular gas mass measurements and describes the analysis of *Chandra* X-ray analysis of the surrounding hot atmospheres. Cluster mass profiles were measured using *Chandra* X-ray and 2MASS infrared data, as shown in Section 3.3.

3.1. Molecular Gas Mass

All objects in our sample were observed with the IRAM 30 m telescope. The cold molecular gas masses for several objects were taken from Edge (2001) and Salomé & Combes (2003), but corrected for a cosmology assuming $\rm H_0 = 70\ km\ s^{-1}\ Mpc^{-1}$. Molecular gas masses for the remaining 26 objects were calculated using recent CO observations from A. C. Edge (2018, in preparation). CO detection for H1821+643 has also been made by Aravena et al. (2011), corresponding to a molecular gas mass of $\sim 8.0 \times 10^9\ M_\odot$. We calculated a molecular gas mass of $\sim 1 \times 10^{10}\ M_\odot$ using line intensity from A. C. Edge (2018, in preparation), and we use this value for our analysis.

Table 2
Data Sample

Cluster	z	X-Ray Core (J2000.0)		BCG Name	BCG Core (J2000.0)	
		α	δ		α	δ
A85	0.055	00:41:50.567	−9:18:10.86	MCG-02-02-086	00:41:50.524	−09:18:10.94
A262	0.017	01:52:46.299	+36:09:11.80	NGC 708	01:52:46.482	+36:09:06.53
A478	0.088	04:13:25.345	+10:27:55.15	2MASX J04132526+1027551	04:13:25.266	+10:27:55.14
A496	0.033	04:33:38.038	−13:15:39.65	MCG-02-12-039	04:33:37.841	−13:15:43.04
A1060	0.013	10:36:42.830	−27:31:39.62	NGC 3311	10:36:42.821	−27:31:42.02
A1068	0.138	10:40:44.520	+39:57:10.28	2MASX J10404446+3957117	10:40:44.504	+39:57:11.26
A1664	0.128	13:03:42.622	−24:14:41.59	2MASX J13034252−2414428	13:03:42.521	−24:14:42.81
A1835	0.253	14:01:01.951	+02:52:43.18	2MASX J14010204+0252423	14:01:02.043	+02:52:42.34
A1991	0.059	14:54:31.553	+18:38:39.79	NGC 5778	14:54:31.465	+18:38:32.57
A2052	0.035	15:16:44.443	+7:01:17.32	UGC 9799	15:16:44.487	+07:01:18.00
A2204	0.152	16:32:46.920	+05:34:32.86	VLSS J1632.7+0534	16:32:46.94	+05:34:32.6
A2597	0.085	23:25:19.779	−12:07:27.63	PKS 2322−12	23:25:19.731	−12:07:27.51
A3581	0.023	14:07:29.791	−27:01:04.06	IC 4374	14:07:29.780	−27:01:04.39
A3880	0.058	22:27:54.455	−30:34:32.88	PKS 2225−308	22:27:54.463	−30:34:32.12
Cygnus-A	0.056	19:59:28.259	+40:44:02.10	Cygnus-A	19:59:28.357	+40:44:02.10
H1821+643	0.297	18:21:57.191	+64:20:36.56	H1821+643	18:21:57.237	+64:20:36.23
Hydra-A	0.055	9:18:05.673	−12:05:43.65	Hydra-A	09:18:05.651	−12:05:43.99
MACS 1532.9+3021	0.345	15:32:53.820	+30:20:59.75	SDSSJ153253.78+302059.3	15:32:53.778	+30:20:59.42
NGC 4325	0.026	12:23:06.659	+10:37:15.53	NGC 4325	12:23:06.672	+10:37:17.05
NGC 5044	0.009	13:15:23.904	−16:23:07.53	NGC 5044	13:15:23.969	−16:23:08.00
PKS 0745−191	0.103	7:47:31.228	−19:17:41.01	PKS 0745−191	07:47:31.296	−19:17:40.34
RXC J0338.6+0958	0.036	3:38:41.055	+9:58:02.26	2MASX J03384056+0958119	3:38:40.579	+9:58:11.78
RXC J0352.9+1941	0.109	3:52:59.001	+19:40:59.81	2MASX J03525901+1940595	3:52:59.016	+19:40:59.59
RX J0821.0+0752	0.110	8:21:02.018	+7:51:47.58	2MASX J08210226+0751479	08:21:02.265	+07:51:47.95
RX J1504.1−0248	0.215	15:04:07.529	−2:48:16.75	2MASX J15040752−0248161	15:04:07.519	−02:48:16.65
RXC J1524.2−3154	0.103	15:24:12.861	−31:54:23.52	2MASX J15241295−3154224	15:24:12.957	−31:54:22.45
RXC J1558.3−1410	0.097	15:58:21.948	−14:09:58.43	PKS 1555−140	15:58:21.948	−14:09:59.05
RX J1350.3+0940	0.090	13:50:21.891	+9:40:10.84	2MASX J13502209+0940109	13:50:22.136	+09:40:10.66
RXC J1459.4−1811	0.236	14:59:28.713	−18:10:45.01	2MASX J14592875−1810453	14:59:28.763	−18:10:45.19
ZwC l1883	0.194	8:42:55.952	+29:27:25.61	2MASX J08425596+2927272	08:42:55.972	+29:27:26.91
ZwC l3146	0.291	10:23:39.741	+4:11:10.64	2MASX J10233960+0411116	10:23:39.609	+04:11:11.68
ZwC l7160	0.258	14:57:15.073	+22:20:35.18	2MASX J14571507+2220341	14:57:15.077	+22:20:34.16
ZwC l8276	0.076	17:44:14.448	+32:59:29.38	2MASX J17441450+3259292	17:44:14.5	+32:59:29
4C+55.16	0.242	8:34:54.917	+55:34:21.44	2MFGC 06756	08:34:54.903	+55:34:21.09
A1668	0.063	13:03:46.602	13:03:46.602	IC 4130	13:03:46.586	+19:16:17.06
A2029	0.077	15:10:56.104	+5:44:41.14	IC 1101	15:10:56.104	+05:44:41.69
A2142	0.091	15:58:20.880	+27:13:44.21	2MASX J15582002+2714000	15:58:20.028	+27:14:00.06
A2151	0.037	16:04:35.758	+17:43:18.54	NGC 6041	16:04:35.757	+17:43:17.20
A2199	0.030	16:28:38.249	+39:33:04.28	NGC 6166	16:28:38.276	+39:33:04.97
A2261	0.224	17:22:27.140	+32:07:57.43	2MASX J17222717+3207571	17:22:27.173	+32:07:57.18
A2319	0.056	19:21:09.638	+43:57:21.53	MCG+07-40-004	19:21:10.049	+43:56:44.32
A2390	0.228	21:53:36.768	+17:41:42.17	2MASX J21533687+1741439	21:53:36.827	+17:41:43.73
A2462	0.073	22:39:11.367	−17:20:28.33	2MASX J22391136−1720284	22:39:11.367	−17:20:28.49
A2634	0.031	23:38:29.426	+27:01:53.86	NGC 7720	23:38:29.390	+27:01:53.53
A2657	0.040	23:44:57.253	+09:11:30.74	2MASX J23445742+0911349	23:44:57.422	+09:11:34.96
A2626	0.055	23:36:30.375	+21:08:48.21	IC 5338	23:36:30.482	+21:08:47.46
A2665	0.056	23:50:50.557	+6:09:03.00	MCG+01-60-039	23:50:50.537	+06:08:58.35
A2734	0.063	0:11:21.665	−28:51:15.05	ESO 409−25	00:11:21.667	−28:51:15.85
A3526	0.011	12:48:48.949	−41:18:43.92	NGC 4696	12:48:49.277	−41:18:39.92
AWM7	0.017	12:30:49.361	+12:23:28.10	NGC 1129	02:54:27.400	+41:34:46.70
M87	0.004	12:30:49.368	+12:23:28.50	M87	12:30:49.423	+12:23:28.04
RX J0439.0+0520	0.208	4:39:02.180	+5:20:43.33	2MASX J04390223+0520443	04:39:02.263	+05:20:43.70
RX J1347.5−1145	0.451	13:47:30.641	−11:45:08.51	GALEX J134730.7−114509	13:47:31.00	−11:45:09.0
ZwC l235	0.083	0:43:52.184	+24:24:20.09	2MASX J00435213+2424213	00:43:52.140	+24:24:21.31
ZwC l2089	0.230	9:00:36.887	+20:53:40.79	2MASX J09003684+2053402	09:00:36.848	+20:53:40.24

Note. BCG coordinates were taken from Hogan et al. (2015).

Line intensities taken from A. C. Edge (2018, in preparation) were determined from measured antenna temperatures and velocity widths found from Gaussian fits to the CO spectra. For the IRAM 30 m telescope, these were converted to integrated flux density $S_{\rm CO}\Delta\nu$ using the following:

$$S_{\rm CO}\Delta\nu({\rm Jy\ km\ s^{-1}}) = [6.8(1+z)^{-1/2}\ {\rm Jy\ K^{-1}}]I_{\rm CO}, \quad (1)$$

where $I_{\rm CO}$ is in units of K km s^{-1} and z is the redshift of the source. Integrated flux density in CO(2−1) or CO(3−2) was

Table 3
X-Ray Observation Properties

Cluster	ObsID	Total Exposure (ks) Raw	Clean
A85	15173, 15174, 16263, 16264, 904	195.2	193.6
A262	2215, 7921	139.4	137.4
A478	1669, 6102	52.4	46.8
A496	4976, 931	94.0	61.7
A1060	2220	31.9	29.4
A1068	1652	26.8	23.2
A1664	1648, 17172, 17173, 17557, 17568, 7901	245.5	233.3
A1835	6880, 6881, 7370	193.7	139.1
A1991	3193	38.3	34.5
A2052	10477, 10478, 10479, 10480, 10879, 10914, 10915, 10916, 10917, 5807, 890	654.0	640.4
A2204	6104, 7940	86.8	80.1
A2597	6934, 7329,922	151.6	137.6
A3581	12884, 1650	91.7	90.6
A3880	5798	22.3	18.6
Cygnus-A	5830, 5831, 6225, 6226, 6228, 6229, 6250, 6252	198.1	193.6
H1821+643	9398, 9845, 9846, 9848	87.0	83.2
Hydra-A	4969, 4970, 576	215.3	186.4
MACS 1532.9+3021	14009, 1649, 1665	108.2	102.4
NGC 4325	3232	30.1	25.7
NGC 5044	9399	82.7	82.5
PKS 0745−191	12881, 1509, 2427, 510	220.6	210.1
RXC J0338.6+0958	7939, 9792	83.3	81.2
RXC J0352.9+1941	10466	27.2	27.2
RX J0821.0+0752	17194, 17563	66.6	63.5
RX J1504.1−0248	17197, 17669, 17670, 4935, 5793	161.7	135.3
RXC J1524.2-3154	9401	40.9	40.9
RXC J1558.3-1410	9402	40.1	35.8
RX J1350.3+0940	14021	19.8	19.4
RXC J1459.4−1811	9428	39.6	39.5
ZwC 11883	2224	29.8	26.3
ZwC 13146	1651, 9371	206.0	189.6
ZwC 17160	4192, 543	101.7	80.0
ZwC 18276	11708, 8267	53.5	53.2
4C+55.16	4940	96.0	65.5
A1668	12877	10.0	10.0
A2029	4977, 6101, 891	107.6	103.3
A2142	15186, 16564, 16565, 5005	199.7	184.6
A2151	4996	21.8	14.4
A2199	10748, 10803, 10804, 10805, 497, 498	158.2	155.8
A2261	5007	24.3	22.1
A2319	15187, 3231	89.6	86.8
A2390	4193, 500, 501	113.9	88.2
A2462	4159	39.2	37.6
A2626	16136, 3192	135.6	132.5
A2634	4816	49.5	47.5
A2657	4941	16.1	15.9
A2665	12280	9.9	9.4
A2734	5797	19.9	18.9
A3526	16223, 16224, 16225, 16534, 16607, 16608, 16609, 16610	486.3	478.5
AWM7	11717, 12016, 12017, 12018	133.8	133.5
M87	5826, 5827	283.0	283.0
RX J0439.0+0520	9369, 9761	28.5	25.9
RX J1347.5−1145	13516, 13999, 14407, 2222, 3592, 506, 507	326.5	286.4
ZwC 12089	10463, 7897	49.7	46.9
ZwC 1235	11735	19.8	19.4

Note. X-ray data were taken from the *Chandra* Data Archive (http://cda.harvard.edu/chaser/).

converted to an equivalent flux density in CO(1−2), assuming flux ratios CO(2−1)/CO(1−0) = 3.2 (David et al. 2014) and CO(3−2)/CO(1−0) = 7.0 (Russell et al. 2016). To translate integrated flux density in CO(1−0) directly to molecular gas mass, we use the formulation taken from Bolatto et al. (2013),

$$M_{\rm mol} = 1.05 \times 10^4 \left(\frac{X_{\rm CO}}{2 \times 10^{20} \frac{\rm cm^{-2}}{\rm K\ km\ s^{-1}}} \right) \frac{S_{\rm CO} \Delta\nu D_{\rm L}^2}{(1+z)}, \quad (2)$$

where $X_{\rm CO}$ is the CO-to-H_2 conversion factor and $D_{\rm L}$ is the luminosity distance in Mpc. Molecular gas mass is sensitive to $X_{\rm CO}$, which is not universal. We adopt the Galactic value $X_{\rm CO} = 2 \times 10^{20}$ cm^{-2} (K km s^{-1})$^{-1}$ with ±30% uncertainty following Bolatto et al. (2013) and previous studies of BCGs in cool core clusters (Edge 2001; Salomé & Combes 2003; McNamara et al. 2014; Russell et al. 2014, 2016; Vantyghem et al. 2016). This value is the mean conversion factor in the Milky Way galaxy. It is lower in the Galactic center and higher at large radii. This $X_{\rm CO}$ value can be approximately applied down to metallicities of $\sim 0.5 Z_\odot$ (Bolatto et al. 2013). The mean metallicity measured for the innermost regions of the hot atmospheres is $0.66 \pm 0.38\ Z_\odot$. Therefore, adopting the Galactic value of $X_{\rm CO}$ is reasonable.

Observations with the ALMA have resolved the spatial and velocity structure of the molecular clouds in several objects in this sample. The molecular gas masses inferred from the IRAM and ALMA observations for the overlapping sample are compared in Table 1. The molecular gas masses inferred from the CO(1−0) transition are generally larger for IRAM observations, suggesting the ALMA observations may have resolved away a fraction of extended CO emission. However, the quality of the ALMA data is superior to the single dish IRAM data, and the measurements from the instruments are consistent to within their uncertainties. Nevertheless, it is reassuring that the two instruments are giving broadly consistent results.

3.2. X-Ray Data Properties

The event data for all observations were obtained from the *Chandra* Data Archive (CDA). Each observation was reprocessed using the CHANDRA_REPRO script with CIAO version 4.7.

Events with bad grades were removed, and background light curves were extracted from the level 2 event files. The events

were filtered using the LC_CLEAN routine of M. Markevitch to identify and remove time intervals affected by flares. Blank-sky backgrounds were extracted using CALDB version 4.6.7 for each observation, reprocessed identically to the event files, and normalized to match the 9.5–12.0 keV count rate in the observations. Calibrated event 2 files (and blank-sky backgrounds) were reprojected to match the position of the observation with the highest clean exposure time. Point sources were identified using WAVDETECT (Freeman et al. 2002), which were visually inspected and then excluded from further analysis.

Spectra were extracted from concentric annuli forming spherical shells using CIAO and binned to a minimum of 30 counts per channel. Following Hogan et al. (2017a), we have taken the location of the BCG as the center for our concentric annuli. To ensure that atmospheric temperature is measured accurately in deprojection, annuli were created with a minimum of ∼3000 net projected counts, with the number per annulus growing with increasing radius. Weighted redistribution matrix files (RMFs) and weighted auxiliary response files (ARFs) were created for each spectrum, using the MKACISRMF and MKWARF, respectively. Lastly, the loss of area to chip gaps and point source extraction regions was corrected in the spectra. These spectra were then deprojected using a geometric routine DSDEPROJ described in Sanders & Fabian (2007) and Russell et al. (2008).

3.2.1. Spectral Fitting and Modeling the ICM

Spectra were modeled with an absorbed single temperature PHABS(MEKAL) thermal model (Mewe et al. 1985, 1986; Balucinska-Church & McCammon 1994; Liedahl et al. 1995; Kaastra 2015) using XSPEC version 12.8.2 (Arnaud 1996). Abundances, anchored to the values in Anders & Grevesse (1989), were allowed to vary in the spectral fits. The hydrogen column density $N_{\rm H}$ was frozen to the value of Kalberla et al. (2005), unless the best fit value was found to be significantly different. Fitting the spectra with the PHABS (MEKAL) model yields values for temperature, metallicity, and XSPEC norm,

$$\mathrm{norm} = \frac{10^{-14}}{4\pi (D_{\rm A}(1+z))^2} \int n_{\rm e} n_{\rm H}\, dV, \qquad (3)$$

where z is redshift, $D_{\rm A}$ is the angular distance to the source, $n_{\rm e}$ and $n_{\rm H}$ are the electron and hydrogen number densities, respectively. Augmenting the previous model to PHABS*CFLUX (MEKAL), we integrate the unabsorbed thermal model between 0.1 and 100 keV and obtain an estimate for the bolometric flux of the X-ray emitting region.

3.2.2. Thermodynamic Properties of the Hot Atmosphere

Electron density was computed using the normalization parameter of the thermal model. Assuming hydrogen and helium mass fractions of $X = 0.75$ and $Y = 0.24$, we find $n_{\rm e} = 1.2 n_{\rm H}$ (Anders & Grevesse 1989). Taking $n_{\rm e}$ and $n_{\rm H}$ to be constant within each spherical shell, the electron density was computed from Equation (3). Bolometric flux of the X-ray emitting region was converted to luminosity $L_{\rm X}$. Pressure and entropy index were computed as $P = 2 n_{\rm e} kT$ and $K = kT n_{\rm e}^{-2/3}$, respectively. In a spherical shell of volume V, the cooling time

Table 4
Mass Parameters

Cluster	σ_* (km s^{-1})	r_s (kpc)	$A = 4\pi G \rho_0 r_s 2 \mu m_{\rm H}$ (keV)	M_{2500} ($10^{13}\ M_\odot$)
A85	270 ± 6	$376.2^{+37.0}_{-25.4}$	$49.1^{+4.0}_{-2.7}$	$22.2^{+1.1}_{-1.2}$
A262	189 ± 3	$185.8^{+3.7}_{-0.4}$	$12.9^{+0.3}_{-0.0}$	$3.4^{+0.1}_{-0.1}$
A478	271 ± 7	$588.2^{+206.8}_{-130.7}$	$71.4^{+18.2}_{-12.4}$	$33.3^{+5.4}_{-6.0}$
A496	228 ± 5	$190.1^{+68.1}_{-38.3}$	$32.8^{+2.5}_{-1.5}$	$12.9^{+1.1}_{-1.1}$
A1060	208 ± 12	191.7	36.9	15.0
A1068	311 ± 12	$519.4^{+122.2}_{-79.8}$	$47.3^{+8.4}_{-5.0}$	$18.5^{+1.8}_{-1.7}$
A1664	267 ± 12	$300.2^{+31.4}_{-29.5}$	$25.7^{+2.3}_{-1.1}$	$8.8^{+0.5}_{-0.5}$
A1835	486 ± 24	$550.3^{+45.3}_{-61.8}$	$94.3^{+5.7}_{-7.7}$	$55.8^{+3.3}_{-3.2}$
A1991	222 ± 8	$266.4^{+93.5}_{-98.9}$	$25.1^{+5.0}_{-6.7}$	$8.5^{+1.5}_{-1.4}$
A2052	221 ± 5	$170.6^{+55.9}_{-39.6}$	$24.8^{+4.1}_{-3.3}$	$8.7^{+1.4}_{-1.4}$
A2204	343 ± 13	$409.6^{+40.6}_{-36.0}$	$80.9^{+5.0}_{-4.3}$	$45.7^{+2.2}_{-2.4}$
A2597	218 ± 10	$257.4^{+52.5}_{-16.9}$	$37.9^{+5.5}_{-2.0}$	$15.1^{+1.6}_{-1.6}$
A3581	195 ± 3	$80.7^{+14.5}_{-13.6}$	$8.4^{+0.5}_{-0.5}$	$2.0^{+0.1}_{-0.1}$
A3880	236 ± 7	$122.1^{+95.3}_{-47.4}$	$21.7^{+4.9}_{-2.8}$	$7.2^{+1.6}_{-1.6}$
Cygnus-A	268 ± 8	$145.0^{+69.9}_{-43.1}$	$45.2^{+4.5}_{-2.1}$	$19.6^{+0.1}_{-0.1}$
H1821+643	250 ± 15[a]	$171.5^{+216.7}_{-15.9}$	$23.1^{+13.6}_{-3.7}$	$7.2^{+2.8}_{-2.7}$
Hydra-A	237 ± 8	$551.8^{+22.7}_{-36.7}$	$37.8^{+0.9}_{-1.4}$	$12.2^{+0.2}_{-0.2}$
MACS 1532.9+3021	250 ± 15	$769.0^{+535.9}_{-144.0}$	$105.2^{+50.0}_{-14.8}$	$43.7^{+7.3}_{-7.5}$
NGC 4325	174 ± 5	$66.2^{+12.4}_{-7.6}$	$4.9^{+0.5}_{-0.3}$	$1.0^{+0.1}_{-0.1}$
NGC 5044	196 ± 11	$45.1^{+5.4}_{-4.7}$	$7.0^{+0.2}_{-0.2}$	$1.5^{+0.1}_{-0.1}$
PKS 0745−191	290 ± 14	$437.9^{+186.1}_{-115.8}$	$67.4^{+18.7}_{-12.5}$	$33.9^{+5.8}_{-5.5}$
RXC J0338.6+0958	220 ± 5	$153.2^{+62.5}_{-59.2}$	$21.3^{+4.6}_{-3.8}$	$7.1^{+1.6}_{-1.5}$
RXC J0352.9+1941	239 ± 10	$223.3^{+37.6}_{-15.0}$	$22.6^{+2.0}_{-0.9}$	$7.5^{+0.4}_{-0.4}$
RX J0821.0+0752	247 ± 9	$268.8^{+453.5}_{-159.1}$	$20.7^{+22.2}_{-7.9}$	$6.5^{+2.8}_{-2.6}$
RX J1504.1−0248	386 ± 22	$787.8^{+142.3}_{-107.2}$	$111.4^{+15.3}_{-12.0}$	$58.6^{+4.6}_{-4.5}$
RXC J1524.2−3154	265 ± 12	$450.5^{+104.3}_{-53.7}$	$64.5^{+11.1}_{-5.3}$	$30.9^{+3.0}_{-2.7}$
RXC J1558.3−1410	280 ± 14	$451.5^{+86.3}_{-89.4}$	$47.5^{+6.3}_{-6.4}$	$19.6^{+1.8}_{-1.8}$
RX J1350.3+0940	188 ± 13	$111.4^{+22.1}_{-59.2}$	$29.3^{+2.2}_{-9.3}$	$9.7^{+1.7}_{-1.8}$
RXC J1459.4−1811	439 ± 22	$421.1^{+128.7}_{-82.1}$	$46.1^{+8.3}_{-6.0}$	$21.6^{+2.1}_{-2.3}$
ZwC 11883	335 ± 12	$315.6^{+196.8}_{-82.1}$	$27.7^{+9.6}_{-4.8}$	$10.3^{+1.4}_{-1.5}$
ZwC 13146	372 ± 33	$719.6^{+104.5}_{-121.6}$	$87.1^{+10.0}_{-11.0}$	$38.2^{+2.9}_{-2.7}$
ZwC 17160	428 ± 21	$455.3^{+102.0}_{-64.2}$	$67.3^{+10.4}_{-7.4}$	$34.4^{+3.3}_{-3.3}$
ZwC 18276	219 ± 7	$531.6^{+59.4}_{-58.5}$	$54.3^{+4.8}_{-4.6}$	$21.5^{+1.2}_{-1.3}$
4C+55.16	274 ± 24	$452.5^{+35.4}_{-27.3}$	$49.4^{+1.8}_{-1.8}$	$18.6^{+1.2}_{-1.1}$
A1668	226 ± 7	$93.7^{+149.9}_{-14.4}$	$13.7^{+15.1}_{-1.2}$	$3.9^{+0.8}_{-0.7}$
A2029	336 ± 10	$511.4^{+50.4}_{-30.9}$	$79.8^{+5.1}_{-3.1}$	$44.8^{+1.8}_{-1.9}$
A2142	241 ± 11	$345.5^{+37.4}_{-21.3}$	$46.8^{+3.0}_{-1.5}$	$20.0^{+0.9}_{-0.8}$
A2151	219 ± 4	$196.0^{+38.7}_{-55.3}$	$15.4^{+1.4}_{-2.3}$	$4.6^{+0.4}_{-0.4}$
A2199	246 ± 4	$364.3^{+181.3}_{-119.4}$	$48.3^{+16.7}_{-11.0}$	$21.6^{+5.3}_{-5.6}$

Table 4
(Continued)

Cluster	σ_* (km s^{-1})	r_s (kpc)	$A = 4\pi G\rho_0 r_s 2\mu m_H$ (keV)	M_{2500} (10^{13} $M_\odot$)
A2261	460 ± 17	$396.6^{+114.4}_{-98.9}$	$77.0^{+13.1}_{-7.4}$	$45.1^{+5.2}_{-4.8}$
A2319	249 ± 7	$397.8^{+110.7}_{-316.9}$	$54.6^{+11.9}_{-41.6}$	$25.2^{+5.0}_{-4.6}$
A2390	348 ± 22	$799.1^{+183.0}_{-79.7}$	$101.3^{+17.8}_{-7.4}$	$47.6^{+3.9}_{-4.0}$
A2462	260 ± 8	$458.7^{+368.9}_{-207.7}$	$28.7^{+14.7}_{-8.5}$	$8.8^{+1.8}_{-1.8}$
A2634	269 ± 3	$133.9^{+63.2}_{-62.7}$	$38.4^{+10.3}_{-13.7}$	$15.9^{+5.5}_{-5.9}$
A2626	243 ± 7	$248.9^{+25.5}_{-25.6}$	$22.1^{+1.3}_{-1.3}$	$7.4^{+0.3}_{-0.3}$
A2657	172 ± 6	$103.8^{+98.6}_{-64.1}$	$8.8^{+2.0}_{-2.8}$	$2.1^{+0.6}_{-0.6}$
A2665	248 ± 7	$613.7^{+464.7}_{-203.9}$	$35.1^{+19.3}_{-8.7}$	$10.0^{+0.0}_{-0.0}$
A2734	231 ± 8	$379.3^{+827.8}_{-110.3}$	$21.1^{+27.0}_{-4.0}$	$5.8^{+1.2}_{-1.2}$
RX J0439.0+0520	389 ± 21	$706.1^{+387.0}_{-237.1}$	$57.7^{+25.8}_{-16.0}$	$22.1^{+4.6}_{-4.3}$
RX J1347.5−1145	250 ± 15[a]	$308.9^{+40.9}_{-31.6}$	$153.5^{+11.7}_{-10.5}$	$94.7^{+7.1}_{-7.1}$
ZwC 1235	240 ± 8	$206.1^{+63.8}_{-39.3}$	$21.4^{+2.3}_{-1.8}$	$7.2^{+0.6}_{-0.5}$
ZwC 12089	296 ± 18	$245.4^{+25.6}_{-28.3}$	$31.6^{+1.4}_{-2.0}$	$11.9^{+0.5}_{-0.6}$

Note. σ_* denotes the equivalent velocity dispersion of the central galaxy inferred from 2MASS isophotal magnitude if the galaxy consisted only of its stars. r_s and ρ_0 denote the characteristic scale radius and density of the NFW profile obtained from the ISONFWMASS model (see Section 3.3). M_{2500} denotes the total cluster mass.
[a] No 2MASS detection. Assigned $\sigma_* = 250$ km s^{-1} following Voit and Donahue (2015).

of the ICM was computed as

$$t_{\rm cool} = \frac{3}{2}\frac{P}{n_e n_H \Lambda(Z, T)} = \frac{3}{2}\frac{PV}{L_X}, \quad (4)$$

where $\Lambda(Z, T)$ is the cooling function as a function of metallicity Z and temperature T. In a shell with electron density n_e, gas density was computed using $\rho_g = 1.2 n_e m_p$, where m_p is the mass of a proton. Finally, to obtain a radial gas mass distribution, gas density profiles were integrated in a piecewise manner from the center of the cluster.

3.3. Mass Profiles

Hydrostatic mass profiles were derived and used to determine gravitational free-fall times and total cluster mass. We adopted the mass model presented in Hogan et al. (2017a). The model is composed of an NFW potential and a central cored isothermal potential representing the central galaxy,

$$\Phi_{\rm NFW} = -4\pi G\rho_0 r_s^2 \frac{\ln(1 + r/r_s)}{r/r_s}$$
$$\Phi_{\rm ISO} = \sigma^2 \ln(1 + (r/r_I)^2), \quad (5)$$

where ρ_0 is the characteristic gas density, r_s is the scale radius of the NFW component, σ is the stellar velocity dispersion, and r_I is the scale radius of the isothermal component. The NFW profile (Navarro et al. 1997) has been found to capture the total gravitating mass of clusters on large scales reasonably well (e.g., Pointecouteau et al. 2005; Vikhlinin et al. 2006; Gitti et al. 2007; Schmidt & Allen 2007; Babyk et al. 2014; Main et al. 2017). However, the NFW profile alone underestimates the inferred mass from the observed velocity dispersion of stars in cluster cores (Fisher et al. 1995; Lauer et al. 2014). The gravitational potential is dominated by the stellar component in the innermost 10–20 kpc (Li & Bryan 2012). The isothermal component of this model accounts for the stellar mass of the central galaxy.

This combined NFW and cored isothermal potential, dubbed ISONFWMASS, is implemented as an extension in the XSPEC package CLMASS (Nulsen et al. 2010). X-ray spectra derived from *Chandra* data are fitted with this model, which assumes that the cluster is spherically symmetric and the gas is in hydrostatic equilibrium. To obtain a stable fit, Hogan et al. (2017a) set the r_I parameter to an arbitrarily small but non-zero value and the σ parameter frozen to an inferred stellar velocity dispersion σ_* derived from 2MASS isophotal K-band magnitudes m_{k20} measured within the isophotal radius r_{k20}.

To determine the uncertainties of these quantities, we have utilized the CHAIN command in XSPEC to generate a chain of sets of parameters via a Markov Chain Monte Carlo (MCMC) method. A chain length of 5000 was produced, from which we adopted the standard deviation as the uncertainty of ρ_0, r_s, and mass profiles. Table 4 shows the fitted parameters for our mass profiles. The free-fall times $t_{\rm ff}$ and total cluster mass proxy M_Δ were then computed as follows:

$$t_{\rm ff} = \sqrt{\frac{2r}{g}} \quad (6)$$

$$M_\Delta = \frac{4\pi R_\Delta^3}{3}\Delta\rho_c, \quad (7)$$

where g is the acceleration due to gravity and $\Delta = 2500$. The values of M_{2500} and R_{2500} were determined from the combined NFW and isothermal profiles by numerically solving Equation (7).

3.4. AGN Mechanical Power

Cavity powers were obtained from the literature for as many objects in our sample as possible (see Table 5 for references). Cavities inflated by radio-emitting jets from the central AGN allow a direct measurement of the mechanical energy output of the AGN. Assuming the cavities are in pressure balance with the surrounding atmosphere, the mean jet power required to create a cavity filled with relativistic gas is at least

$$P_{\rm cav} = \frac{4PV}{t_{\rm age}}, \quad (8)$$

where V is the volume of the cavity, P is the surrounding pressure, and $t_{\rm age}$ is the age of the cavity, estimated by using the cavity's buoyancy time (time required for the cavity to rise buoyantly at its terminal velocity). In total, we found cavity power measurements from the literature for 27 objects in our sample.

A less reliable method for probing the mechanical output of an AGN is to use a correlation between its radio luminosity and cavity power. We derive mechanical power inferred from the AGN's radio luminosity using (Bîrzan et al. 2008)

$$\log P_{\rm mech} = (0.48 \pm 0.07)\log L_{\rm radio} + (2.32 \pm 0.09), \quad (9)$$

Table 5
Cavity Power and Star Formation Rate

Cluster	L_{radio} (10^{37} erg s^{-1})	Cavity Power		$L_{H\alpha}$ (10^{40} erg s^{-1})	Star Formation		Reference
		P_{mech} (10^{42} erg s^{-1})	P_{cav} (10^{42} erg s^{-1})		$SFR_{H\alpha}$ ($M_\odot$ yr^{-1})	SFR_{IR} ($M_\odot$ yr^{-1})	
A85	2550 ± 110	35.9 ± 1.7	$37.0^{+37.0}_{-11.0}$	0.43	0.033 ± 0.010	1.57	[1], [2]
A262	277 ± 10	12.4 ± 2.3	$9.7^{+7.5}_{-2.6}$	0.43	0.033 ± 0.010	0.55	[1], [3]
A478	4420 ± 176	46.7 ± 0.5	$100.0^{+80.0}_{-20.0}$	7.86	1.453 ± 0.186	···	[1], [3]
A496	1840 ± 65	30.7 ± 2.1	172.0	0.72	0.065 ± 0.017	···	[14], [2]
A1060	1.7 ± 1.1	1.1 ± 0.5	0.261	···	···	···	[14], -
A1068	6814 ± 214	57.5 ± 1.1	20.0	121.43	51.039 ± 2.878	187.45	[1], [3]
A1664	9678 ± 316	68.1 ± 3.0	$95.2^{+74.0}_{-74.0}$	78.57	28.982 ± 1.862	14.54	[4], [3]
A1835	37100	129.8 ± 19.2	$1800.0^{+1900.0}_{-600.0}$	100.00	39.654 ± 2.370	···	[1], [3]
A1991	1973 ± 65	31.7 ± 2.1	86.4	0.60	0.051 ± 0.014	<1.66	[11], [2]
A2052	97400 ± 3700	206.3 ± 47.0	$150.0^{+200.0}_{-70.0}$	1.38	0.151 ± 0.033	1.37	[1], [2]
A2204	26700 ± 991	110.9 ± 13.5	50000	114.29	47.171 ± 2.709	14.62	[15], [3]
A2597	205300 ± 6160	295.1 ± 86.7	$67.0^{+87.0}_{-29.0}$	37.14	10.943 ± 0.880	···	[1], [3]
A3581	4720 ± 166	48.2 ± 0.3	3.1	21.30	5.311 ± 0.505	···	[9], [2]
A3880	11300 ± 342	73.4 ± 4.1	$29.0^{+36.2}_{-23.8}$	···	···	···	[5], -
Cygnus-A	72800000 ± 1870000	4939.9 ± 4699.6	$1300.0^{+1100.0}_{-200.0}$	21.30	5.311 ± 0.505	···	[1], [2]
H1821+643	<5990	<54.1 ± 0.6	No Cavity	···	···	···	[12], -
Hydra-A	1710000 ± 54500	816.5 ± 408.9	$430.0^{+200.0}_{-50.0}$	11.43	2.364 ± 0.271	···	[1], [3]
MACS 1532.9+3021	56400 ± 1940	158.7 ± 28.9	$2220.0^{+860.0}_{-860.0}$	300.01	165.407 ± 7.110	96.15	[10], [3]
NGC 4325	<32.1	<4.4 ± 1.3	···	0.36	0.026 ± 0.008	<0.66	-, [7]
NGC 5044	42.0 ± 1.7	5.0 ± 1.4	$4.2^{+1.2}_{-2.0}$	···	···	···	[8], -
PKS 0745−191	387000 ± 13700	400.2 ± 141.1	$1700.0^{+1400.0}_{-300.0}$	140.00	61.411 ± 3.318	17.07	[1], [6]
RXC J0338.6+0958	706 ± 35	19.4 ± 2.5	$24.0^{+23.0}_{-6.0}$	7.14	1.283 ± 0.169	2.09	[1], [3]
RXC J0352.9+1941	<648	<18.6 ± 2.5	No Cavity	41.43	12.612 ± 0.982	11.04	[12], [3]
RX J0821.0+0752	728	19.7 ± 2.5	···	30.00	8.290 ± 0.711	36.91	-, [6]
RX J1504.1−0248	50800 ± 2140	150.9 ± 26.1	···	···	···	···	-, -
RXC J1524.2−3154	8180 ± 261	62.8 ± 2.0	$239.0^{+122.0}_{-122.0}$	···	···	···	[5], -
RXC J1558.3−1410	66500 ± 2350	171.8 ± 33.6	$44.5^{+26.7}_{-26.7}$	···	···	···	[5], -
RX J1350.3+0940	36000 ± 1100	128.0 ± 18.6	···	···	···	···	-, -
RXC J1459.4−1811	107000 ± 3230	215.5 ± 50.8	No Cavity	···	···	···	[12], -
ZwC l1883	16400 ± 587	87.8 ± 7.4	···	···	···	···	-, -
ZwC l3146	12000 ± 814	75.6 ± 4.6	$5800.0^{+6800.0}_{-1500.0}$	500.01	321.332 ± 11.850	···	[1], [3]
ZwC l7160	19700 ± 124	95.7 ± 9.4	···	35.72	10.399 ± 0.846	···	-, [3]
ZwC l8276	7850 ± 282	61.6 ± 1.8	···	9.29	1.805 ± 0.220	3.71	-, [3]
4C+55.16	8870000 ± 266000	1799.3 ± 1230.9	$420.0^{+440.0}_{-160.0}$	71.43	25.605 ± 1.693	···	[1], [3]
A1668	4630 ± 141	47.8 ± 0.4	···	12.00	2.519 ± 0.284	<1.66	-, [6]
A2029	48200 ± 1850	147.2 ± 24.9	$87.0^{+49.0}_{-4.0}$	0.80	0.075 ± 0.019	···	[1], [6]
A2142	<440	<15.4 ± 2.4	No Cavity	···	···	···	[12], -
A2151	207	10.8 ± 2.2	···	5.80	0.979 ± 0.137	···	-, [6]
A2199	46700 ± 1560	144.9 ± 24.1	$270.0^{+250.0}_{-60.0}$	3.50	0.508 ± 0.083	···	[1], [6]
A2261	3060	39.2 ± 1.4	···	···	···	···	-, -
A2319	<157	<9.4 ± 2.0	···	10.00	1.987 ± 0.237	···	-, [6]
A2390	221000 ± 7770	305.7 ± 91.8	No Cavity	44.29	13.754 ± 1.050	···	[12], [7]
A2462	<279	<12.4 ± 2.3	···	5.80	0.979 ± 0.137	···	-, [6]
A2634	103000	211.6 ± 49.2	···	3.70	0.546 ± 0.088	···	-,[6]
A2657	<80.1	<6.8 ± 1.7	···	0.17	0.010 ± 0.004	···	-, [2]
A2626	2480 ± 111	35.4 ± 1.8	···	3.30	0.470 ± 0.078	<1.66	[5], [6]
A2665	2520 ± 94	35.7 ± 1.8	···	0.60	0.051 ± 0.014	<1.66	-, [6]
A2734	651 ± 34	18.6 ± 2.5	···	···	···	···	-, -
A3526	7010 ± 194	58.3 ± 1.3	No Cavity	0.36	0.026 ± 0.008	···	[13], [3]
AWM7	<14.2	<3.0 ± 1.0	···	0.36	0.026 ± 0.008	···	-, [3]
M87	34100 ± 1210	124.6 ± 17.6	···	0.79	0.073 ± 0.019	···	-, [3]
RX J0439.0+0520	85000 ± 2990	193.3 ± 41.8	···	78.57	28.982 ± 1.862	18.66	-, [3]
RX J1347.5−1145	217000 ± 8650	302.9 ± 90.5	No Cavity	214.29	106.805 ± 5.079	···	[12], [3]
ZwC l235	5170 ± 166	50.4 ± 0.0	···	2.93	0.403 ± 0.069	<1.66	-, [7]
ZwC l2089	8980 ± 573	65.7 ± 2.6	···	71.43	25.605 ± 1.693	270.47	-, [3]

Note. Hα luminosities were taken from Edge (2001); Salomé and Combes (2003); and the ACCEPT database (Donahue et al. 2006; Cavagnolo et al. 2009). We then use these Hα luminosities to calculate $SFR_{H\alpha}(M_\odot yr^{-1}) = 7.9 \times 10^{-42} L_{H\alpha}(\mathrm{erg\ s^{-1}})$ (Kennicutt 1998), which is corrected for reddening using $2.7 \times SFR^{1.3}$ (Kewley et al. 2002). Star formation rates derived from IR luminosities (SFR_{IR}) were taken from O'Dea et al. (2008). References for P_{cav} or $L_{H\alpha}$ are as follows: [1] Rafferty et al. (2006), [2] ACCEPT Database Cavagnolo et al. (2009), [3] Edge (2001), [4] Kirkpatrick et al. (2009), [5] J. Hlavacek-Larrondo (2014, private communication), [6] Salomé and Combes (2003), [7] Crawford et al. (1999), [8] Cavagnolo et al. (2010), [9] Canning et al. (2013), [10] Hlavacek-Larrondo et al. (2013), [11] Pandge et al. (2013), [12] Shin et al. (2016), [13] Panagoulia et al. (2014), [14] Bîrzan et al. (2012), [15] Sanders et al. (2009). The P_{cav} for A496 and A1060 were computed using pV and t_{buoy} from [14] and the formula $P_{cav} = 4\mathrm{pV}/t_{buoy}$.

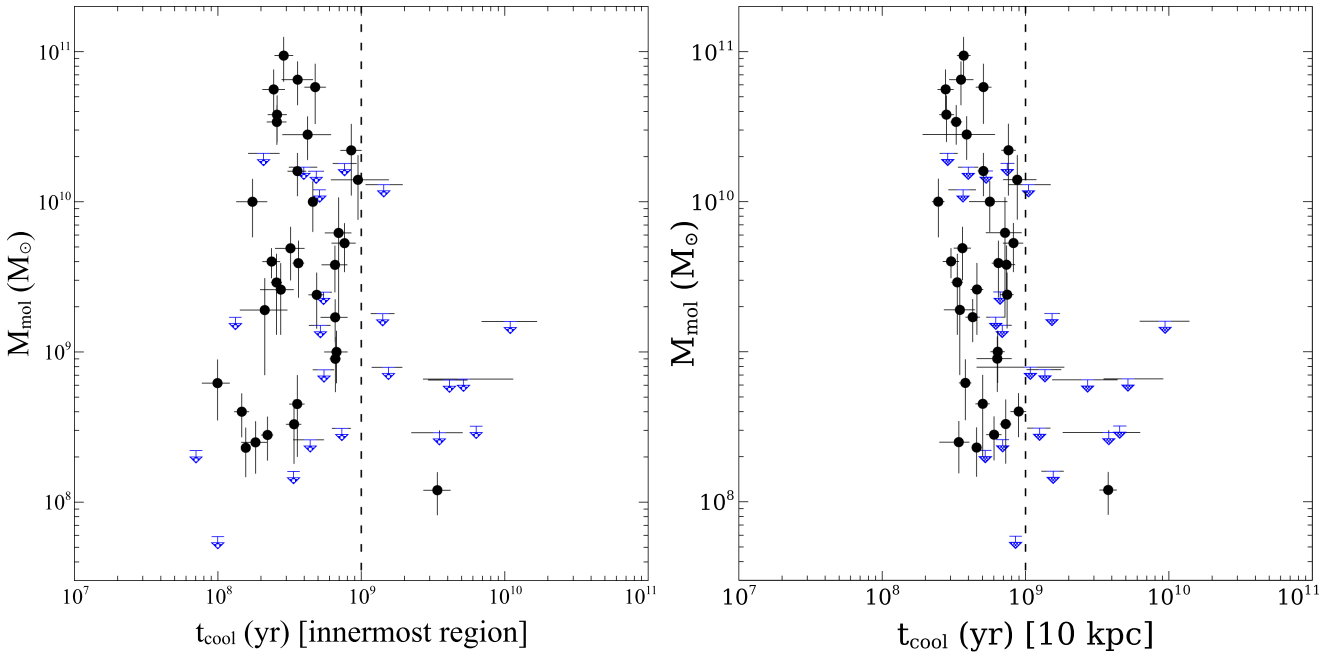

Figure 2. Molecular gas mass vs. cooling time measured at the mean radius of the innermost region (left panel) and the cooling time measured at 10 kpc (right panel). Circular symbols denote systems observed with CO emission while arrow symbols denote upper limits.

where the total radio luminosity was calculated by integrating the flux between $\nu_1 = 10$ MHz and $\nu_2 = 5000$ MHz as

$$L_{\rm rad} = 4\pi D_{\rm L}^2 S_{\nu_0} \int_{\nu_1}^{\nu_2} (\nu/\nu_0)^{-\alpha} d\nu, \qquad (10)$$

following Bîrzan et al. (2004). We used a spectral index of $\alpha \approx 0.75$, assuming a power-law spectrum $S_\nu \sim \nu^{-\alpha}$. We have taken the $\nu_0 = 1400$ MHz flux reported in the NRAO VLA Sky Survey (NVSS) Catalog (Condon et al. 2002). Table 5 shows the mechanical power inferred from radio luminosities for objects in our sample.

4. Results

4.1. Cooling Time and Molecular Gas

In this section, we investigate whether and how the cooling time of the atmosphere is related to the molecular gas found in the central galaxies. Star formation and nebular emission in central galaxies ensues when the cooling time falls below $\sim 10^9$ years, a phenomenon known as the cooling time threshold (Cavagnolo et al. 2008; Rafferty et al. 2008; Hogan et al. 2017b). As star formation is strongly coupled to molecular gas mass, we study the relationship between molecular gas and cooling time.

Molecular gas mass is plotted against central cooling time in the left panel of Figure 2. Because we have more than one molecular gas mass estimate for some of the systems in our sample and that we favor the most recent CO data from (A. C. Edge 2018, in preparation), we plot the estimates calculated from CO line intensities taken from (A. C. Edge 2018, in preparation) when available. Otherwise, we plot the recomputed estimates from Edge (2001) and Salomé and Combes (2003).

Due to the large range in cluster distances, the innermost bins do not sample the same linear diameters. This resolution effect is seen in Figure 3, which shows the central cooling time

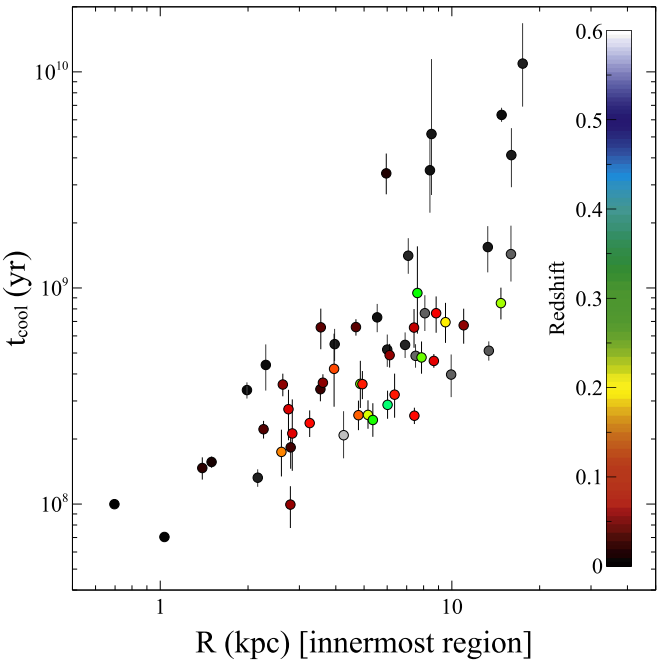

Figure 3. Cooling time in the innermost region plotted against the mean radius of the innermost region. The tendency of the cooling time to increase with size of the innermost region is easily observed in this figure.

against the mean radius of the innermost region, $R_{\rm mid} = (R_{\rm inner} + R_{\rm outer})/2$. The plot shows a tendency to measure lower central cooling times with smaller $R_{\rm mid}$. This is consistent with the findings of Peres et al. (1998) and Hogan et al. (2017b), who observed a trend of reduced central cooling time with increased resolution for the sample as a whole. This bias is not only related to the resolution of the optics combined with the sources distance. An accurate gas temperature measurement requires a minimum number of counts per bin or annulus.

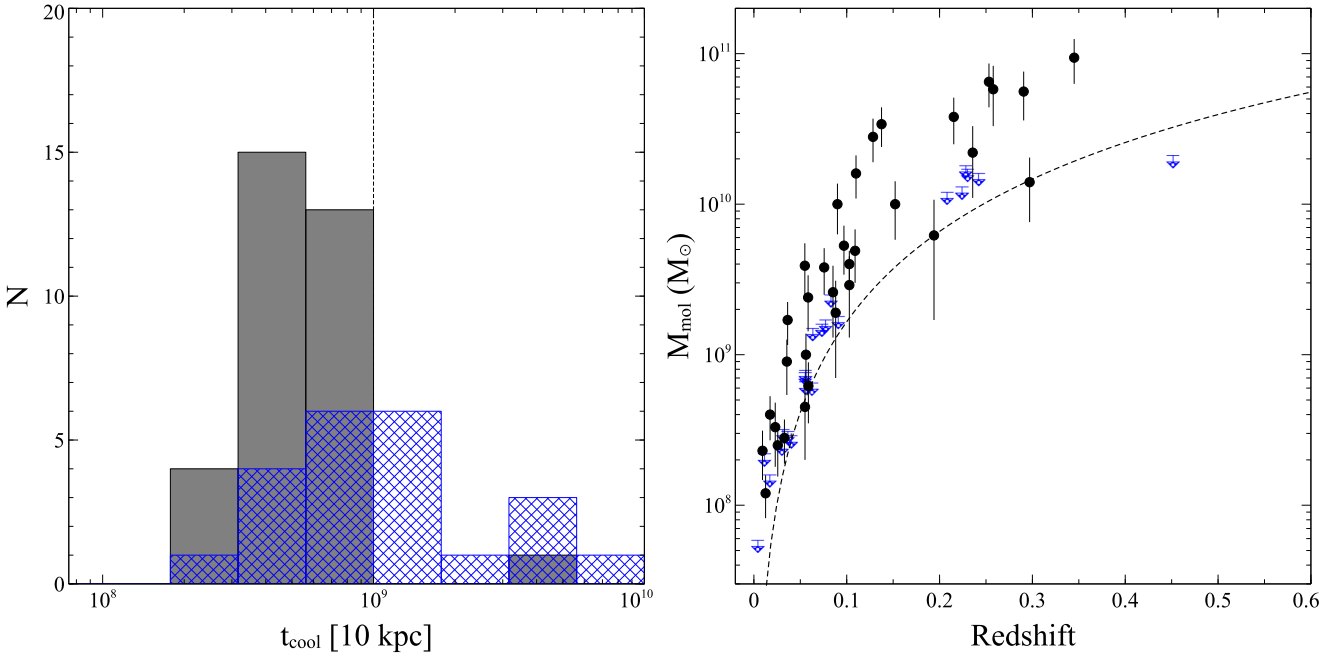

Figure 4. Left: histogram of the cooling times at 10 kpc. Gray bars denote clusters detected in CO while blue bars denote non-detection. Right: molecular gas mass vs. redshift. The dashed curve represents the molecular mass limit that can be derived from CO(1−0) observations with the IRAM 30 m telescope, assuming a typical 300 km s^{-1} linewidth and main beam temperature detection limit of 0.5 mK. The molecular gas mass for the two systems below this curve were derived from CO(3−2) observations. Black symbols denote systems observed with CO emission, while blue symbols denote upper limits.

Therefore, the effective resolution depends also on the surface brightness of the atmosphere and the exposure time. To account for this resolution bias, the right panel of Figure 2 shows the cooling time at a single physical radius of 10 kpc. Those systems whose innermost regions have $R_{\rm mid} > 10$ kpc were extrapolated to 10 kpc using the linear slope of the first two points in the radial profile in log–log space. There are eight such systems in our sample. Among these systems, the largest value found for $R_{\rm mid}$ is 17.5 kpc. When cooling times are plotted at a standard altitude of 10 kpc in the right panel of Figure 2, the distribution of cooling times narrows, so that cooling times falling below 2×10^8 years are not observed. This shows that the larger variation in cooling time seen in the left panel is due to resolution.

The sudden jump in molecular gas mass seen in Figure 2 shows that molecular gas resides preferentially in systems with central cooling times lying below ∼1 Gyr. Central galaxies located in clusters with longer central cooling times contain less than $\sim 10^9\ M_\odot$ of molecular gas. The molecular gas masses in central galaxies with atmospheric cooling times lying below 1 Gyr at 10 kpc rise dramatically to several $10^{10}\ M_\odot$. Molecular gas masses of this magnitude dramatically exceed those in gas-rich spirals like the Milky Way. Furthermore, we find a narrow spread in cooling time below ∼1 Gyr with a mean of 0.5 Gyr and a standard deviation of 0.2 Gyr.

Figure 2 shows the same ∼1 Gyr cooling time threshold for the onset of molecular gas that has previously been found in Hα emission and star formation. This threshold suggests that molecular gas is linked to hot atmospheres with short cooling times, consistent with the hypothesis that molecular clouds in central galaxies condense from hot atmospheres.

The histogram of central cooling times (see the left panel of Figure 4) shows two classes of outliers in the cooling time plot: (1) the system Abell 1060 with long central cooling time, yet with detectable levels of molecular gas, and (2) 11 systems with short central cooling times but only upper limits to their molecular gas masses. The latter imply that a short cooling time does not guarantee the detection of molecular gas via CO emission. We consider these exceptions in turn.

Consistent with our findings, Abell 1060 was previously classified as a "weak" cool core (1 Gyr $< t_{\rm cool} <$ 7.7 Gyr; Mittal et al. 2009). Accordingly, its molecular gas mass $1.2 \times 10^8 \pm 0.4\ M_\odot$ is the lowest of the sample. As expected, this value lies at the low end of the range of molecular gas typically observed in central galaxies ($\sim 10^{8-11}\ M_{\rm mol}$, Edge 2001; Salomé & Combes 2003), but well into the regime of molecular gas observed in normal elliptical galaxies ($\sim 10^{7-9}\ M_{\rm mol}$ Young et al. 2011). Abell 1060 may have accumulated its molecular gas through a merger or perhaps through atmospheric cooling at an earlier time when its atmosphere was denser or AGN feedback was less effective. The origin of molecular gas in elliptical galaxies is poorly understood. It may originate from both external (from another galaxy) and internal (stellar mass loss) processes (Young et al. 2011).

Next, we address systems with short cooling times lacking CO detections. In the left panel of Figure 4, the detections (black) and non-detections (blue) occupy similar distributions in $t_{\rm cool}$. A Kolmogorov–Smirnov test gives a p-value of 0.22, which is too large to reject the null hypothesis that they were drawn from the same parent distribution. It is then possible and even likely that molecular gas is present but falls below the detection limit of the IRAM 30 m observations.

The right panel of Figure 4 shows molecular gas mass plotted against redshift. The dashed line represents the molecular mass limit that can be achieved from our CO(1−0) observations with the IRAM telescope. Due to this detection limit, molecular clouds with CO(1−0) line emission below this curve will not be detectable. The distribution of upper limits is consistent with the detections, indicating that these objects

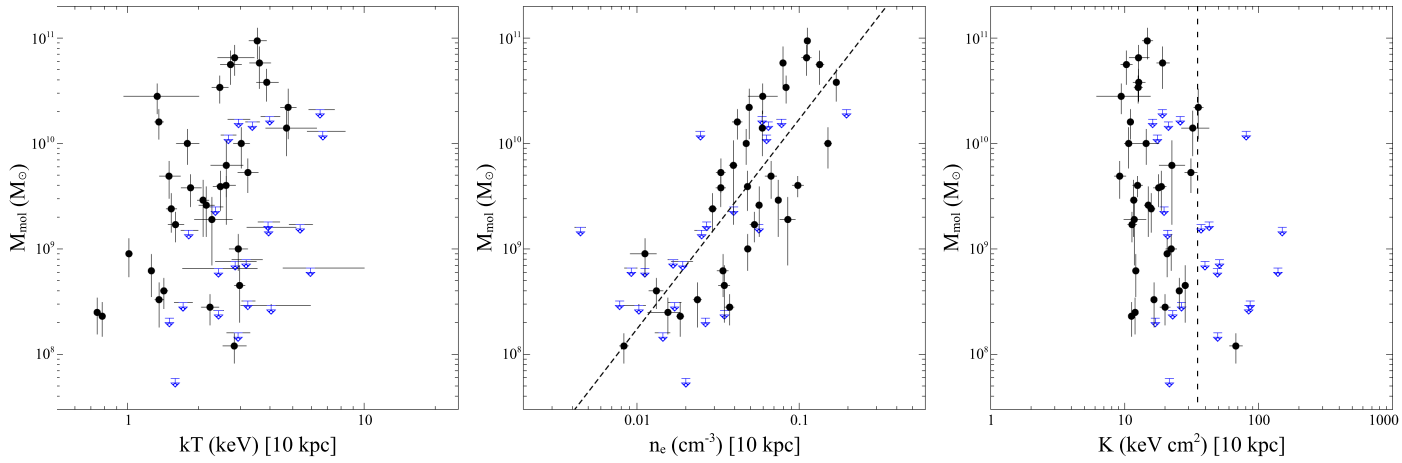

Figure 5. Molecular gas mass vs. temperature, density, and entropy derived at 10 kpc. Black symbols denote systems observed with CO emission, while blue symbols denote upper limits. In the middle panel, the dashed black line is a fit only to the systems with CO detection.

likely contain substantial levels of molecular gas that lie below our detection limits. Alternatively, their molecular gas levels may be suppressed, perhaps due to AGN feedback. The connection between molecular gas and AGN feedback will be explored further in Section 5.2.

4.2. Correlations between Thermodynamic Parameters and Molecular Gas

Understanding the relationship between the hot atmosphere and molecular gas is one of the goals of this paper. We have investigated the dependence of molecular gas mass with atmospheric temperature, density, and entropy in Figure 5. The quantities are evaluated at 10 kpc to avoid resolution bias. While we find no obvious correlation between molecular gas mass and temperature, molecular gas mass and atmospheric density are strongly correlated. We find the best fit for the systems with CO detections only to be ($R^2 = 0.60$)

$$\log M_{\rm mol} = (1.99 \pm 0.51)\log n_{\rm e} + (12.22 \pm 0.70). \quad (11)$$

The trend shows that molecular gas mass increases with atmospheric gas density, consistent with an atmospheric origin for the molecular gas. Discussed in more detail in Section 5.2, higher ICM densities require greater heating to offset radiative cooling, hence a larger pool of molecular gas to feed the AGN.

The trend between molecular gas mass and entropy ($K = kTn_{\rm e}^{-2/3}$) shown in the third panel of Figure 5 shows that molecular gas is found in large quantities only in systems when the entropy falls below $\sim$35 keV cm^2. The only outlier yet again is Abell 1060, as discussed earlier. Like cooling time, a low entropy atmosphere does not guarantee a detection of molecular gas. Furthermore, a narrow spread is observed in the entropy distribution below $\sim$35 keV cm^2 with a mean of 17 keV cm^2 and standard deviation of 7 keV cm^2. These characteristics mirror those found for cooling time alone.

4.3. Ratio of Cooling to Free-fall Time

Atmospheric gas should become unstable to cooling when its ratio of the cooling to free-fall time ($t_{\rm cool}/t_{\rm ff}$) falls below $\sim$1 (Nulsen 1986; McCourt et al. 2012). This criterion may rise above 10 in real atmospheres (Gaspari et al. 2012; Sharma et al. 2012; Gaspari et al. 2013; Voit & Donahue 2015), which we investigate here. Our analysis closely mirrors that of Hogan et al. (2017b), who adopted nebular emission rather than CO to trace cold gas. Likewise our results and conclusions are similar.

The left panel of Figure 6 shows molecular gas mass plotted against the cooling time of the atmosphere at the radius, $R_{\rm min}$, where the minimum ratio of $t_{\rm cool}/t_{\rm ff}$ is found. The spread of cooling time for objects detected with molecular gas has a mean $\mu \simeq 0.46$ Gyr and standard deviation $\sigma \simeq 0.19$ Gyr.

The right panel is similar, but the cooling time is divided by the free-fall time at $R_{\rm min}$. Objects with detectable levels of molecular gas lie in the interval $10 \lesssim \min(t_{\rm cool}/t_{\rm ff}) \lesssim 25$. The cutoffs on the high and low end of this range are abrupt. The discontinuity at 25 corresponds roughly to the 1 Gyr threshold in cooling time found here and in Rafferty et al. (2006) and Cavagnolo et al. (2008). The lower cutoff at 10 is similar to that found by Hogan et al. (2017b) and Voit et al. (2015a). Two to four points fall just below 10 in this figure, but not significantly below when noise in the $t_{\rm cool}/t_{\rm ff}$ profile is taken into account (Hogan et al. 2017b, but see Prasad et al. 2015).

With a mean of 13.8 and a standard deviation of 4.6, the distribution of $t_{\rm cool}/t_{\rm ff} < 25$ appears narrower than the distribution of $t_{\rm cool}$ alone. This narrowing suggests that the free-fall time is contributing an observable and perhaps physical effect on the onset of thermally unstable cooling.

However, the narrow spread of $\min(t_{\rm cool}/t_{\rm ff})$, found also by Hogan et al. (2017b), can be attributed to a resolution bias. To demonstrate this bias, the minimum value of the ratio is plotted against its numerator and denominator in Figure 7. The points are color-coded by the value of $R_{\rm min}$.

This figure reveals two key points: first, $\min(t_{\rm cool}/t_{\rm ff})$ is positively correlated with its numerator and denominator. The coefficients of determination, R^2, are 0.82 and 0.35, respectively. The stronger correlation with cooling time is evident over the entire range of $\min(t_{\rm cool}/t_{\rm ff})$. Conversely, the correlation with free-fall time vanishes for $\min(t_{\rm cool}/t_{\rm ff}) < 35$, where cooling is strongest. These trends show that $t_{\rm cool}$ is primarily determining the $\min(t_{\rm cool}/t_{\rm ff})$ ratio. McNamara et al. (2016) and Hogan et al. (2017b) reached the same conclusion.

Second, the measured value of $\min(t_{\rm cool}/t_{\rm ff})$ correlates with $R_{\rm min}$. This trend is seen clearly in the right panel of Figure 7, where we plot the numerator against the denominator of $\min(t_{\rm cool}/t_{\rm ff})$ with points color-coded by $R_{\rm min}$. For a given value of $\min(t_{\rm cool}/t_{\rm ff})$, a large numerator is offset by a large denominator, and conversely so. In other words, the narrow distribution of $\min(t_{\rm cool}/t_{\rm ff})$ is plausibly explained by a

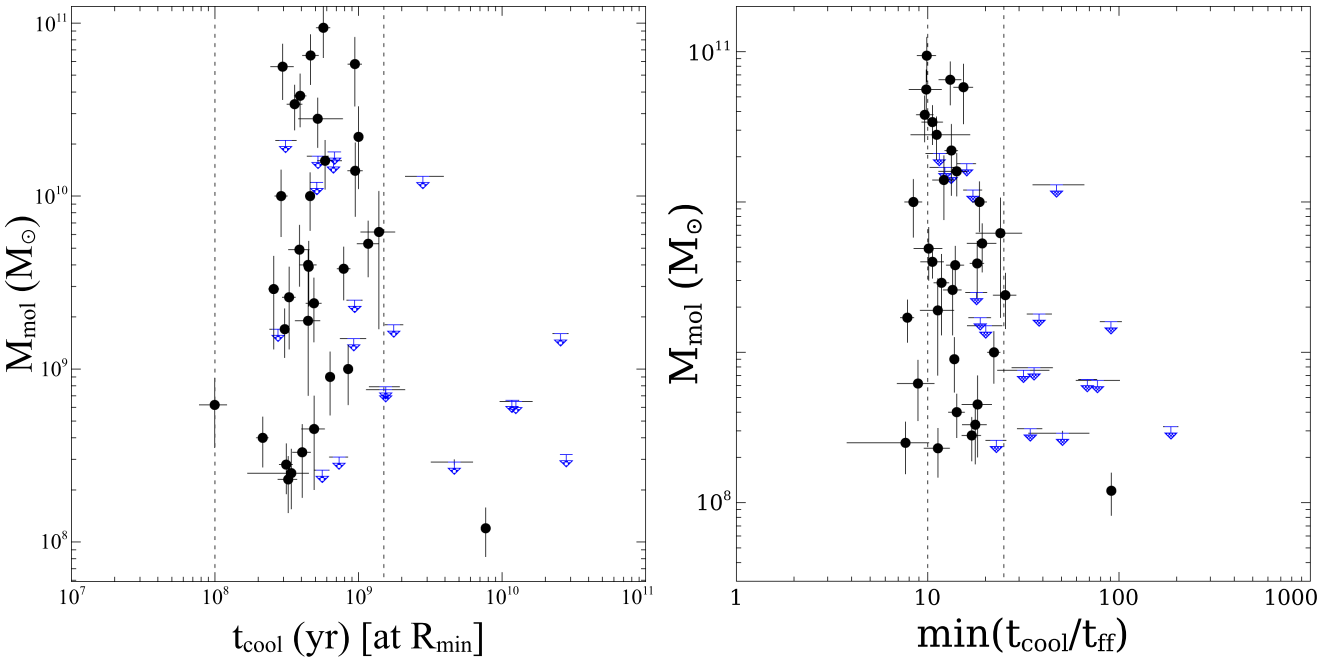

Figure 6. Left panel: molecular gas mass vs. cooling time of the hot atmosphere at the radius at which the minimum of cooling to free-fall time occurs. Right panel: molecular gas mass vs. minimum cooling to free-fall time ratio.

resolution bias. Shorter cooling times are always measured closer to the nucleus where the free-fall time is likewise shorter. The converse is also true. The upshot is that $\min(t_{\rm cool}/t_{\rm ff})$ is condemned to lie in a narrow range because of how it is defined. A similar conclusion was reached by Hogan et al. (2017b).

Hogan et al. (2017b) also considered the possibility that the minimum in the $t_{\rm cool}/t_{\rm ff}$ profiles may actually be a floor, rather than a clear minimum with an upturn at smaller radii. When the mass profile is approximately isothermal and the entropy profile follows a power-law slope of $K \propto r^{2/3}$ in the inner region, $t_{\rm cool}/t_{\rm ff} \propto 1/[\Lambda(kT)^{1/2}]$ is found (Hogan et al. 2017b). This expression is independent of radius, suggesting that the upturns observed in $t_{\rm cool}/t_{\rm ff}$ profiles are produced by density inhomogeneous along the line of sight (Hogan et al. 2017b).

In summary, we preferentially observe objects with molecular gas when the cooling to free-fall time ratio lies in the narrow range $10 \lesssim \min(t_{\rm cool}/t_{\rm ff}) \lesssim 25$. The upper bound corresponds to the $\sim$1 Gyr cooling time threshold; no object falls significantly below 10. The narrow spread can be attributed to resolution bias, although a physical origin cannot be ruled out.

4.4. Does Thermally Unstable Cooling Ensue When $t_{cool}/t_{ff} \lesssim 10$?

Thermally unstable cooling in a stratified, plane-parallel atmosphere is thought to occur when the ratio of the local cooling time to free-fall time, $t_{\rm cool}/t_{\rm ff}$, falls below unity (McCourt et al. 2012). Recent studies have suggested that this ratio rises above unity in realistic, three-dimensional atmospheres (Gaspari et al. 2012; McCourt et al. 2012; Li et al. 2015; Prasad et al. 2015; Singh & Sharma 2015; Voit et al. 2015a; Voit & Donahue 2015; Lakhchaura et al. 2016). For example, Voit and Donahue (2015) found that nebular emission became prevalent in systems where $4 \lesssim \min(t_{\rm cool}/t_{\rm ff}) \lesssim 20$. Numerical feedback simulations by Li et al. (2015) found that atmospheres become thermally unstable when $1 \lesssim \min(t_{\rm cool}/t_{\rm ff}) \lesssim 25$. These studies suggest that those systems with $t_{\rm cool}/t_{\rm ff}$ lying below 10 are rapidly cooling into molecular clouds, while the atmospheres of those lying above 10 are stabilized by AGN feedback (Gaspari et al. 2012; Voit et al. 2017b).

The measurements shown in Figure 6 are broadly consistent with this statement. There is little doubt that the molecular clouds formed from thermally unstable cooling. But significant and consequential issues remain:

1. First, the cycling of heating and cooling that may lead to large fluctuations in central atmospheric gas density and cooling time is not observed here or by Hogan et al. (2017b). Because the gravitational potentials are fixed, only the cooling time may be varying. Our data show the cooling time varies much less than contemplated by Li et al. (2015) and Voit et al. (2017b). For example, over the course of their 6 Gyr simulation, Li et al. (2015) found that this ratio falls below 10 about one-fifth of the time. We would then expect that of the 55 clusters observed here, roughly 10 should lie below $\min(t_{\rm cool}/t_{\rm ff}) < 10$. This number would increase to 20, were we to include the Hogan et al. (2017b) sample. Only two to four objects fall just below 10, and no object falls significantly below.

   This discrepancy is unlikely due to sampling bias. We have explored a wide range of AGN power (10^{42-46} erg s^{-1}), halo mass ($M_{2500} \sim 10^{13-14}\ M_\odot$), molecular gas mass ($10^{8-11}\ M_\odot$), and redshift ($z \sim$ 0–0.4). We should be sampling the entire feedback cycle of heating and cooling contemplated by Li et al. (2015) and others.

   The upshot is that our measurements are in tension with models that assume molecular gas forms from local thermal instability growing from linear density perturbations (McCourt et al. 2012; Sharma et al. 2012). Figure 6 shows that systems rich in molecular gas lie in the range $10 < t_{\rm cool}/t_{\rm ff} < 25$, the regime where atmospheres are

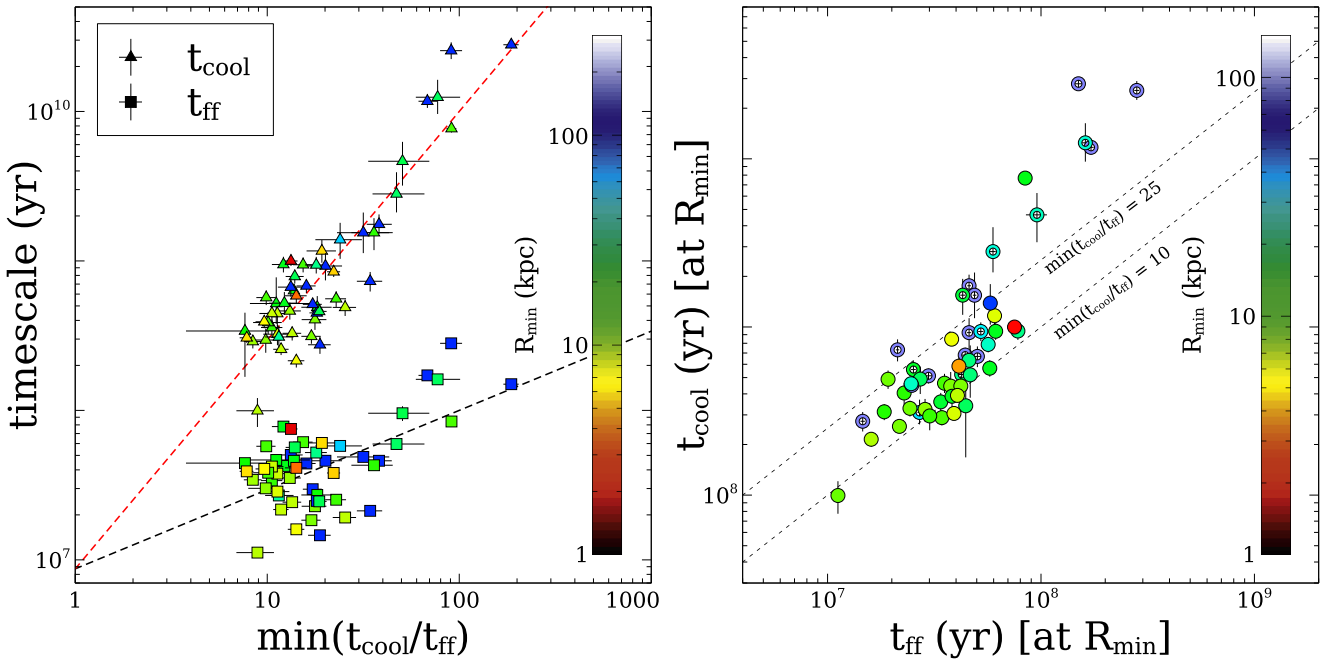

Figure 7. Left panel: minimum cooling to free-fall time plotted against its numerator and denominator for our sample. The red and black dashed lines are linear fit in log–log space to the numerator and denominator against the ratio, respectively. Right panel: the numerator plotted against denominator of the $\min(t_{\rm cool}/t_{\rm ff})$ ratio. In both plots, the points are color-coded by the radius at which the minimum of the $\min(t_{\rm cool}/t_{\rm ff})$ occurs.

expected to be stable to condensation (Gaspari et al. 2012). Nevertheless, ALMA observations of many systems indicate that molecular gas is condensing currently on a timescale shorter than the free-fall timescale.

Many cluster simulations show large temperature, density, and entropy fluctuations in response to AGN activity that damp away over several tens to hundreds of Myer. However, in real clusters, feedback is unrelenting. Cluster atmospheres would not settle before the next significant AGN outburst. Feedback is a gentle process. Host atmospheres remain remarkably stable throughout the feedback cycle and over large variations in jet power (McNamara et al. 2016; Hogan et al. 2017b). Simulations have begun to incorporate this into feedback models (Hillel & Soker 2016; Yang & Reynolds 2016; Gaspari & Sądowski 2017; Meece et al. 2017; Ruszkowski et al. 2017). Solving this problem will surely lead to new insights into the subtlety of self regulation.

2. All systems with molecular gas detections lie in the narrow range $10 \lesssim \min(t_{\rm cool}/t_{\rm ff}) \lesssim 25$. We find no indication that atmospheres hosting systems with the largest molecular gas reservoirs lie preferentially at the low end, and presumably more thermally unstable end, of $\min(t_{\rm cool}/t_{\rm ff})$. The most powerful jets are not associated with larger molecular gas reservoirs (Figure 9), nor does jet power correlate with higher values of $\min(t_{\rm cool}/t_{\rm ff})$ (Figure 10).

   The most general observation that can be made is that thermally unstable cooling ensues when the cooling time of the atmosphere drops below $\sim$1 Gyr, or $\min(t_{\rm cool}/t_{\rm ff}) \lesssim 25$, or $K \lesssim 35$ keV cm^2. Measurements provide no further indication of the role the free-fall time plays, as the value of the ratio is driven almost entirely by the cooling time (McNamara et al. 2016; Hogan et al. 2017b).

3. Finally, the Voit et al. (2017b) precipitation model assumes cluster entropy profiles become isentropic (constant entropy) in their centers. This occurs where the $t_{\rm cool}/t_{\rm ff}$ ratio reaches a minimum value $t_{\rm cool}/t_{\rm ff} \lesssim 10$ at the outer radius of the isentropic region. The absence of an entropy gradient in the isentropic region would promote thermally unstable cooling without the aid of uplift from the radio AGN. This mechanism, in principle, could supply fuel to the nuclear regions of galaxies that lie below the resolution limits of X-ray observations.

   However, observation provides little indication that they do. Entropy profiles for several nearby ellipticals (Werner et al. 2012, 2014; Voit et al. 2015b) that probe below 1 kpc flatten in the inner 100 parsecs or so and may become constant. However, this flattening is seen only in the inner one or two bins where the temperature and density profiles are poorly resolved. Isentropic cores on larger scales are rare (Panagoulia et al. 2014; Hogan et al. 2017b). Instead, the entropy profiles scale approximately as $K \propto r^{2/3}$ in the inner few tens of kpc. Hogan et al. (2017b) pointed out that this scaling naturally leads to a $t_{\rm cool}/t_{\rm ff}$ profile that reaches a constant in the inner few tens of kpc. This region is prone cooling that may be stimulated by uplift (McNamara et al. 2016; Voit et al. 2017b), consistent with ALMA molecular gas observations.

5. Discussion

5.1. Cooling Out of the Hot Atmosphere as a Plausible Origin of Cold Gas

Molecular gas in early-type galaxies rarely rises above $\sim 10^8\,M_\odot$ (Young et al. 2011). However, many central cluster galaxies are exceptionally rich in molecular gas, with masses approaching $\sim 10^{11}\,M_\odot$ in some instances. Studies have shown that nebular emission and star formation in central galaxies are

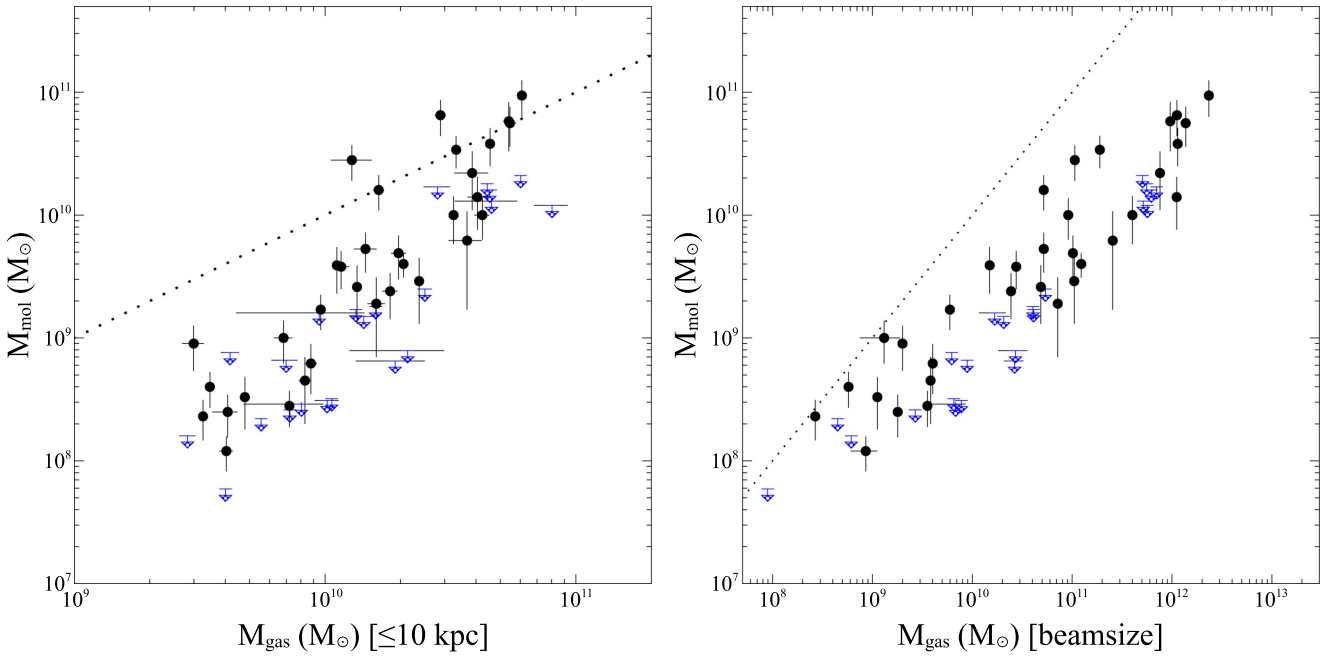

Figure 8. Left panel: molecular gas mass enclosed within the IRAM 30 m beam vs. hot gas mass enclosed within 10 kpc in radius from the cluster core. Right panel: molecular gas mass vs. hot gas mass both enclosed within the IRAM 30 m beam. The dotted line shows equality of the quantities. Black symbols denote systems observed with CO emission, while blue symbols denote upper limits.

correlated with short central cooling times of the hot intracluster medium. For example, systems with Hα emission and blue continuum emission have been preferentially detected with central cooling times $\lesssim$1 Gyr and entropy index $\lesssim$30 keV cm^2 (Cavagnolo et al. 2008; Rafferty et al. 2008; Voit & Donahue 2015). While Hα and blue light trace the cold 10^4 K ionized gas and recent star formation, respectively, CO emission probes the gas, directly fueling star formation and AGN. Molecular gas drives galaxy and black hole co-evolution. If the molecular clouds have indeed cooled from hot atmospheres, mass continuity dictates that their hot reservoirs must be significantly more massive than the molecular reservoirs in central galaxies.

On the left panel in Figure 8, we plot molecular gas mass against the surrounding atmospheric mass observed in the inner 10 kpc, where most of the molecular gas is seen by ALMA. Two features are seen in this plot. First, the atmospheric mass is positively correlated with the molecular gas mass. Second, in most instances the atmospheric mass exceeds the molecular gas mass. Taking the atmospheric gas mass within the beam (right panel of Figure 8), the average fraction of cold to hot gas within the beam is 0.18 on average. This trend is consistent with the density trend shown in Figure 5. Both are plausible, with the molecular gas having cooled from the hot atmosphere. In some cases, such as Abell 1835, the molecular gas mass exceeds the atmospheric mass in its vicinity. The single dish beam of IRAM for A1835 is roughly 104 kpc and measures a molecular to atmospheric gas ratio of $6.5 \times 10^{10}\ M_\odot / 1.1 \times 10^{12}\ M_\odot \approx 0.06$. However, within 10 kpc of its BCG, ALMA observations measure this ratio to be $5 \times 10^{10}\ M_\odot / 1.12 \times 10^{10}\ M_\odot \approx 4.46$. In the few cases where this is true, the gas likely cooled from larger radii or has lingered over time. On the whole, these trends would be difficult to explain by an external origin, such as a merger or stripping from a plunging galaxy.

The left panel of Figure 9 plots the depletion timescale for star formation to consume the molecular gas. The median depletion timescale is ~1 Gyr (see also O'Dea et al. 2008). Taken at face value, the depletion timescales indicated long-lived star formation. Long-lived star formation is in tension with the molecular gas kinematics, discussed below.

5.2. A Relationship between Molecular Gas and AGN Feedback?

AGN power roughly balances energetically the radiative losses from the atmospheres (e.g., Bîrzan et al. 2004). This balance can be maintained only if accretion onto the black hole responds promptly to a change of atmospheric state. Accretion from the hot atmosphere surrounding the nuclear black hole should occur at some level (Allen et al. 2006). Bondi accretion alone would be insufficient to fuel the most powerful AGN if their nuclear black hole masses follow the $M - \sigma$ relation (Rafferty et al. 2006; Hardcastle et al. 2007; McNamara et al. 2011; Narayan & Fabian 2011). On the other hand, molecular gas is abundant and could easily supply the fuel, found here and elsewhere (Pizzolato & Soker 2005; Gaspari et al. 2012; Li & Bryan 2014; Prasad et al. 2015).

Assuming hot atmospheres are stabilized by AGN feedback, higher atmospheric gas densities would require higher heating levels. Furthermore, systems with higher atmospheric gas densities would likewise require larger molecular gas reservoirs to fuel AGN (middle panel of Figure 5). We would then expect molecular gas mass to correlate with AGN power.

The right panel of Figure 9 reveals no strong correlation between these quantities. We instead observe a 3 decade scatter in AGN power for a given molecular gas mass. Taken at face value, this figure is inconsistent with molecular gas fueling of AGN feedback. However, in a similar analysis, McNamara et al. (2011) pointed out that only a small fraction of the molecular gas near the nucleus would be required to fuel the AGN at the observed power levels. The single dish masses given here are sensitive to molecular gas spread over tens of kiloparsecs. Therefore these measurements do not have the spatial sensitivity to reveal such a correlation, should it exist.

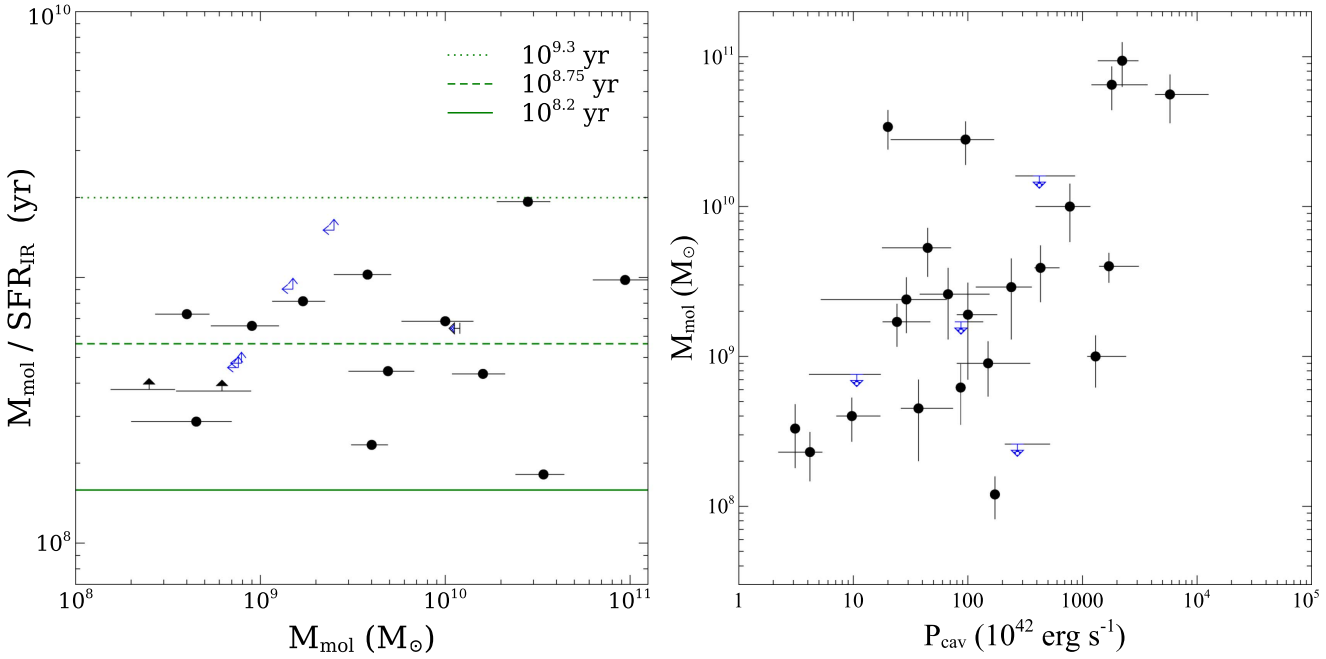

Figure 9. Left panel: depletion timescale of molecular gas due to star formation (M_{mol}/SFR_{IR}) vs. molecular gas mass. Star formation rates were taken from O'Dea et al. (2008). Right panel: molecular gas mass vs. cavity power. Black symbols denote systems observed with CO emission, while blue symbols denote upper limits.

Nevertheless, such a correlation should exist and should be pursued with high resolution ALMA measurements.

5.3. Molecular Gas Stimulated by Uplift?

Molecular gas maps of more than a half dozen systems show a surprising level of complexity (Salomé & Combes 2003; David et al. 2014; McNamara et al. 2014; Russell et al. 2014, 2017, 2016, 2017; Tremblay et al. 2016; Vantyghem et al. 2016). Apart from Hydra-A (Hamer et al. 2014), ordered motion in disks or rings is largely absent. Instead the molecular gas lies in filaments and lumps that are often displaced from the center of the host galaxy. Their velocities and velocity dispersions are surprisingly low. Molecular clouds in central galaxies are often moving well below both the free-fall speed and the velocity dispersions of the stars. Their low velocities and disordered motions suggest the clouds are young and have only recently cooled from the surrounding atmosphere. These properties are difficult to square, with the long, ~1 Gyr depletion timescale to star formation seen in Figure 9.

In many systems, the molecular gas is projected behind buoyantly rising X-ray bubbles. Examples include Perseus (Lim et al. 2008; Salomé et al. 2008), Phoenix (Russell et al. 2017), Abell 1835 (McNamara et al. 2014), PKS 0745−091 (Russell et al. 2016), and Abell 1795 (Russell et al. 2017). This phenomenology indicates that the molecular clouds are being tossed around by rising X-ray bubbles or molecular cloud condensation is initiated by cool atmospheric gas lifted to higher altitudes in the wakes of buoyantly rising X-ray bubbles (Revaz et al. 2008; Li & Bryan 2014; McNamara et al. 2014; Brighenti et al. 2015; McNamara et al. 2016; Voit et al. 2017b). Both mechanisms are occurring at some level.

ALMA observations are providing clues to why hot atmospheres become thermally unstable when $\min(t_{cool}/t_{ff})$ lies well above 10. Indications are that uplift plays a central role. ALMA has shown that molecular clouds are moving well

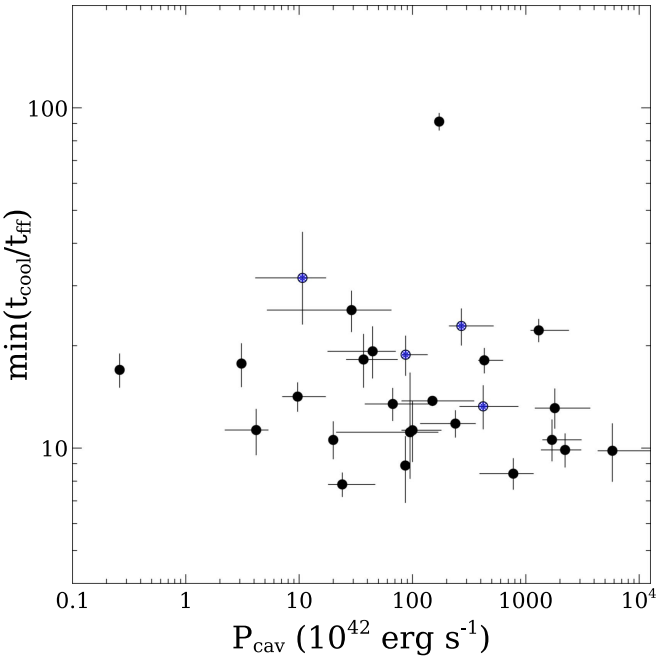

Figure 10. Minimum cooling to free-fall ratio vs. cavity power. Black symbols denote systems observed with CO emission, while blue symbols denote upper limits.

below free-fall speeds. Motivated by these results, we suggested in McNamara et al. (2016) that lifting parcels of gas that then fall inward in less than the free-fall speed can promote thermally unstable cooling, pushing $\min(t_{cool}/t_I)$ toward unity. Infall timescales may be significantly larger than the free-fall timescale, with the limiting timescale governed by the terminal speed of the clouds. This conjecture, which we

have dubbed "stimulated feedback," posits that the AGN itself stimulates the cooling that fuels it. Similarly, Pizzolato and Soker (2005) suggested that inhomogeneities created by jets and bubbles would initiate nonlinear cooling, eventually leading to molecular gas condensation. Voit et al. (2017b) have added an uplift mechanism to their precipitation model. While uplift has emerged as a significant element of thermally unstable cooling, the relevance of the minimum value of $t_{\rm cool}/t_{\rm ff}$ to thermally unstable cooling is, in our view, less clear. This conjecture is difficult to test because the gravitational potential wells of elliptical and BCGs are so similar that the free-fall timescales are nearly identical from system to system (Hogan et al. 2017b). Therefore, most studies have exaggerated the correlation between $t_{\rm cool}/t_{\rm ff}$ and thermally unstable cooling, which is instead driven by the cooling time. We cannot exclude a central role for the free-fall time. But observation provides little indication that a specific value or range of this ratio is driving factor.

Feedback stimulated by uplift may be a general phenomenon. Cooling may be stimulated by any mechanism that lifts low entropy gas out from the core of a galaxy. Mechanisms include rising radio bubbles, jets, or atmospheric sloshing initiated by a merger.

6. Summary

We investigated the molecular cloud properties of 55 central cluster galaxies with molecular gas masses lying between 10^8 and $10^{11}\,M_\odot$. *Chandra* X-ray observations were used to measure cluster mass profiles into the central 10 kpc of the clusters accounting for the mass of the central galaxy. Acceleration profiles, temperature, density, and other thermodynamic parameters were used to examine the possibility that the molecular gas formed through thermally unstable cooling from the hot atmosphere.

1. Molecular gas at levels between $10^9\,M_\odot$ and $10^{11}\,M_\odot$ is preferentially observed in BCGs with cooling times less than 1 Gyr, or entropy index below 35 cm^2 at a resolved radius of 10 kpc. The corresponding star formation rates lie between 0.55 and 270 $M_\odot$ yr^{-1}.
2. Molecular gas mass is strongly and positively correlated with both central atmospheric gas density and atmospheric gas mass. These trends are consistent with the molecular clouds having condensed from the hot atmospheres.
3. The molecular gas depletion timescales due to star formation lie below 1 Gyr. The average depletion timescale $\simeq 5\times10^8$ years is a constant independent of molecular gas mass. This long timescale is in tension with ALMA observations, showing the molecular gas has formed recently and has not relaxed to a dynamically stable configuration such as a disk or ring.
4. Central galaxies rich in molecular gas lie in the range $10 \lesssim \min(t_{\rm cool}/t_{\rm ff}) \lesssim 25$. This small observed range can be plausibly attributed to an observational selection effect, although real physical effects cannot be excluded. The range is inconsistent with models positing that thermally unstable cooling ensues when $\min(t_{\rm cool}/t_{\rm ff}) \lesssim 10$, but is broadly consistent with the range found in chaotic cold accretion models (Gaspari et al. 2012).
5. Large fluctuations in the central atmospheric gas density and temperature in response to AGN activity found in many feedback models are absent. Accordingly, no correlation between $\min(t_{\rm cool}/t_{\rm ff})$ and molecular gas mass is found.
6. The tendency for molecular clouds to lie behind buoyantly rising X-ray bubbles suggests the molecular gas is being lifted directly and/or is condensing from thermally unstable gas being lifted by the bubbles. We suggested here and elsewhere that the feedback loop may be stimulated by uplift from the X-ray bubbles themselves, and in some instances by ram pressure induced by atmospheric sloshing.

B.R.M. acknowledges funding from the Natural Science and Engineering Research Council of Canada and from the Canadian Space Agency. A.C.E. acknowledges support from STFC grant ST/P00541/1. We would also like to thank Noam Soker and Max Gaspari for their comments. A special thanks is extended to the referee, Mark Voit, whose challenges strengthened the paper. H.R.R. acknowledges support from ERC Advanced Grant Feedback 340442. Support for this work was provided in part by the National Aeronautics and Space Administration through *Chandra* Award Number G05-16134X, issued by the *Chandra* X-Ray Observatory Center, which is operated by the Smithsonian Astrophysical Observatory for and on behalf of the National Aeronautics Space Administration under contract NAS8-03060. We also acknowledge IRAM observers Pierre Hily-Blant, Richard Wilman, Stephen Hamer, and Raymond Oonk. The scientific results reported in this article are based on observations made by the *Chandra* X-Ray Observatory (CXO), Institut de Radioastronomie Millimétrique (IRAM) 30 m telescope, and Two Micron All Sky Survey (2MASS). The following software from the *Chandra* X-Ray Center (CXC) has been used: CIAO, ChIPs, and Sherpa. This research has also made use of the NASA/IPAC Extragalactic Database (NED). The plots in this paper were created using Veusz by Jeremy Sanders.

ORCID iDs

F. A. Pulido https://orcid.org/0000-0003-3595-937X
B. R. McNamara https://orcid.org/0000-0002-2622-2627
A. C. Edge https://orcid.org/0000-0002-3398-6916
M. T. Hogan https://orcid.org/0000-0002-7031-721X
A. N. Vantyghem https://orcid.org/0000-0003-4227-4838
P. E. J. Nulsen https://orcid.org/0000-0003-0297-4493
I. Babyk https://orcid.org/0000-0003-3165-9804

References

Allen, S. W., Dunn, R. J. H., Fabian, A. C., Taylor, G. B., & Reynolds, C. S. 2006, MNRAS, 372, 21
Anders, E., & Grevesse, N. 1989, GeCoA, 53, 197
Aravena, M., Wagg, J., Papadopoulos, P. P., & Feain, I. J. 2011, ApJ, 737, 64
Arnaud, K. A. 1996, in ASP Conf. Ser. 101, Astronomical Data Analysis Software and Systems V, ed. G. H. Jacoby & J. Barnes (San Francisco, CA: ASP), 17
Babyk, Y. V., Del Popolo, A., & Vavilova, I. B. 2014, ARep, 58, 587
Baldry, I. K., Glazebrook, K., Brinkmann, J., et al. 2004, ApJ, 600, 681
Balucinska-Church, M., & McCammon, D. 1994, yCat, 6062, 0
Bîrzan, L., McNamara, B. R., Nulsen, P. E. J., Carilli, C. L., & Wise, M. W. 2008, ApJ, 686, 859
Bîrzan, L., Rafferty, D. A., McNamara, B. R., Wise, M. W., & Nulsen, P. E. J. 2004, ApJ, 607, 800

Bîrzan, L., Rafferty, D. A., Nulsen, P. E. J., et al. 2012, MNRAS, 427, 3468
Bolatto, A. D., Wolfire, M., & Leroy, A. K. 2013, ARA&A, 51, 207
Bregman, J. N., Fabian, A. C., Miller, E. D., & Irwin, J. A. 2006, ApJ, 642, 746
Bregman, J. N., & Hogg, D. E. 1988, AJ, 96, 455
Brighenti, F., Mathews, W. G., & Temi, P. 2015, ApJ, 802, 118
Canning, R. E. A., Sun, M., Sanders, J. S., et al. 2013, MNRAS, 435, 1108
Cavagnolo, K. W., Donahue, M., Voit, G. M., & Sun, M. 2008, ApJL, 683, L107
Cavagnolo, K. W., Donahue, M., Voit, G. M., & Sun, M. 2009, ApJS, 182, 12
Cavagnolo, K. W., McNamara, B. R., Nulsen, P. E. J., et al. 2010, ApJ, 720, 1066
Choudhury, P. P., & Sharma, P. 2016, MNRAS, 457, 2554
Condon, J. J., Cotton, W. D., Greisen, E. W., et al. 2002, yCat, 8065, 0
Crawford, C. S., Allen, S. W., Ebeling, H., Edge, A. C., & Fabian, A. C. 1999, MNRAS, 306, 857
David, L. P., Lim, J., Forman, W., et al. 2014, ApJ, 792, 94
Donahue, M., Horner, D. J., Cavagnolo, K. W., & Voit, G. M. 2006, ApJ, 643, 730
Edge, A. C. 2001, MNRAS, 328, 762
Edge, A. C., & Frayer, D. T. 2003, ApJL, 594, L13
Edge, A. C., Wilman, R. J., Johnstone, R. M., et al. 2002, MNRAS, 337, 49
Faber, S. M., Willmer, C. N. A., Wolf, C., et al. 2007, ApJ, 665, 265
Fabian, A. C. 1994, in NATO Advanced Science Institutes (ASI) Series C, Vol. 441, ed. W. C. Seitter (Berlin: Springer), 163
Fabian, A. C. 2012, ARA&A, 50, 455
Fisher, D., Illingworth, G., & Franx, M. 1995, ApJ, 438, 539
Freeman, P. E., Kashyap, V., Rosner, R., & Lamb, D. Q. 2002, ApJS, 138, 185
Gaspari, M., Ruszkowski, M., & Oh, S. P. 2013, MNRAS, 432, 3401
Gaspari, M., Ruszkowski, M., & Sharma, P. 2012, ApJ, 746, 94
Gaspari, M., & Sądowski, A. 2017, ApJ, 837, 149
Gitti, M., McNamara, B. R., Nulsen, P. E. J., & Wise, M. W. 2007, ApJ, 660, 1118
Grabelsky, D. A., & Ulmer, M. P. 1990, ApJ, 355, 401
Hamer, S. L., Edge, A. C., Swinbank, A. M., et al. 2014, MNRAS, 437, 862
Hardcastle, M. J., Evans, D. A., & Croston, J. H. 2007, MNRAS, 376, 1849
Hillel, S., & Soker, N. 2016, MNRAS, 455, 2139
Hlavacek-Larrondo, J., Allen, S. W., Taylor, G. B., et al. 2013, ApJ, 777, 163
Hogan, M. T., Edge, A. C., Hlavacek-Larrondo, J., et al. 2015, MNRAS, 453, 1201
Hogan, M. T., McNamara, B. R., Pulido, F., et al. 2017a, ApJ, 837, 51
Hogan, M. T., McNamara, B. R., Pulido, F., et al. 2017b, ApJ, 851, 66
Kaastra, J. S. 2015, IAUGA, 22, 2249812
Kalberla, P. M. W., Burton, W. B., Hartmann, D., et al. 2005, A&A, 440, 775
Kennicutt, R. C., Jr. 1998, ARA&A, 36, 189
Kewley, L. J., Geller, M. J., Jansen, R. A., & Dopita, M. A. 2002, AJ, 124, 3135
Kirkpatrick, C. C., McNamara, B. R., Rafferty, D. A., et al. 2009, ApJ, 697, 867
Lakhchaura, K., Saini, T. D., & Sharma, P. 2016, MNRAS, 460, 2625
Lauer, T. R., Postman, M., Strauss, M. A., Graves, G. J., & Chisari, N. E. 2014, ApJ, 797, 82
Lazareff, B., Castets, A., Kim, D.-W., & Jura, M. 1989, ApJL, 336, L13
Leroy, A. K., Walter, F., Brinks, E., et al. 2008, AJ, 136, 2782
Li, Y., & Bryan, G. L. 2012, ApJ, 747, 26
Li, Y., & Bryan, G. L. 2014, ApJ, 789, 54
Li, Y., Bryan, G. L., Ruszkowski, M., et al. 2015, ApJ, 811, 73
Liedahl, D. A., Osterheld, A. L., & Goldstein, W. H. 1995, ApJL, 438, L115
Lim, J., Ao, Y. & Dinh-V-Trung 2008, ApJ, 672, 252
Main, R. A., McNamara, B. R., Nulsen, P. E. J., Russell, H. R., & Vantyghem, A. N. 2017, MNRAS, 464, 4360
McCourt, M., Sharma, P., Quataert, E., & Parrish, I. J. 2012, MNRAS, 419, 3319
McNamara, B. R., & Jaffe, W. 1994, A&A, 281, 673
McNamara, B. R., & Nulsen, P. E. J. 2007, ARA&A, 45, 117
McNamara, B. R., & Nulsen, P. E. J. 2012, NJPh, 14, 055023
McNamara, B. R., Rohanizadegan, M., & Nulsen, P. E. J. 2011, ApJ, 727, 39
McNamara, B. R., Russell, H. R., Nulsen, P. E. J., et al. 2014, ApJ, 785, 44
McNamara, B. R., Russell, H. R., Nulsen, P. E. J., et al. 2016, ApJ, 830, 79
Meece, G. R., Voit, G. M., & O'Shea, B. W. 2017, ApJ, 841, 133
Mewe, R., Gronenschild, E. H. B. M., & van den Oord, G. H. J. 1985, A&AS, 62, 197
Mewe, R., Lemen, J. R., & van den Oord, G. H. J. 1986, A&AS, 65, 511
Mirabel, I. F., Sanders, D. B., & Kazes, I. 1989, ApJL, 340, L9
Mittal, R., Hudson, D. S., Reiprich, T. H., & Clarke, T. 2009, A&A, 501, 835
Narayan, R., & Fabian, A. C. 2011, MNRAS, 415, 3721
Navarro, J. F., Frenk, C. S., & White, S. D. M. 1997, ApJ, 490, 493
Nulsen, P. E. J. 1986, MNRAS, 221, 377
Nulsen, P. E. J., Powell, S. L., & Vikhlinin, A. 2010, ApJ, 722, 55
O'Dea, C. P., Baum, S. A., Maloney, P. R., Tacconi, L. J., & Sparks, W. B. 1994, ApJ, 422, 467
O'Dea, C. P., Baum, S. A., Privon, G., et al. 2008, ApJ, 681, 1035
O'Dea, C. P., Payne, H. E., & Kocevski, D. 1998, AJ, 116, 623
Panagoulia, E. K., Fabian, A. C., Sanders, J. S., & Hlavacek-Larrondo, J. 2014, MNRAS, 444, 1236
Pandge, M. B., Vagshette, N. D., Sonkamble, S. S., & Patil, M. K. 2013, Ap&SS, 345, 183
Peres, C. B., Fabian, A. C., Edge, A. C., et al. 1998, MNRAS, 298, 416
Peterson, J. R., Kahn, S. M., Paerels, F. B. S., et al. 2003, ApJ, 590, 207
Pizzolato, F., & Soker, N. 2005, ApJ, 632, 821
Pointecouteau, E., Arnaud, M., & Pratt, G. W. 2005, A&A, 435, 1
Prasad, D., Sharma, P., & Babul, A. 2015, ApJ, 811, 108
Prasad, D., Sharma, P., & Babul, A. 2017, MNRAS, 471, 1531
Rafferty, D. A., McNamara, B. R., & Nulsen, P. E. J. 2008, ApJ, 687, 899
Rafferty, D. A., McNamara, B. R., Nulsen, P. E. J., & Wise, M. W. 2006, ApJ, 652, 216
Revaz, Y., Combes, F., & Salomé, P. 2008, A&A, 477, L33
Russell, H. R., McDonald, M., McNamara, B. R., et al. 2017, ApJ, 836, 130
Russell, H. R., McNamara, B. R., Edge, A. C., et al. 2014, ApJ, 784, 78
Russell, H. R., McNamara, B. R., Fabian, A. C., et al. 2016, MNRAS, 458, 3134
Russell, H. R., Sanders, J. S., & Fabian, A. C. 2008, MNRAS, 390, 1207
Ruszkowski, M., Yang, H.-Y. K., & Reynolds, C. S. 2017, ApJ, 844, 13
Salomé, P., & Combes, F. 2003, A&A, 412, 657
Salomé, P., Combes, F., Revaz, Y., et al. 2008, A&A, 484, 317
Sanders, J. S., & Fabian, A. C. 2007, MNRAS, 381, 1381
Sanders, J. S., Fabian, A. C., & Taylor, G. B. 2009, MNRAS, 393, 71
Schmidt, R. W., & Allen, S. W. 2007, MNRAS, 379, 209
Sharma, P., McCourt, M., Quataert, E., & Parrish, I. J. 2012, MNRAS, 420, 3174
Shin, J., Woo, J.-H., & Mulchaey, J. S. 2016, ApJS, 227, 31
Singh, A., & Sharma, P. 2015, MNRAS, 446, 1895
Strateva, I., Ivezić, Ž, Knapp, G. R., et al. 2001, AJ, 122, 1861
Thomas, D., Maraston, C., Bender, R., & Mendes de Oliveira, C. 2005, ApJ, 621, 673
Tremblay, G. R., Oonk, J. B. R., Combes, F., et al. 2016, Natur, 534, 218
Vantyghem, A. N., McNamara, B. R., Russell, H. R., et al. 2016, ApJ, 832, 148
Vikhlinin, A., Kravtsov, A., Forman, W., et al. 2006, ApJ, 640, 691
Voit, G. M., & Donahue, M. 2015, ApJL, 799, L1
Voit, G. M., Donahue, M., Bryan, G. L., & McDonald, M. 2015a, Natur, 519, 203
Voit, G. M., Donahue, M., O'Shea, B. W., et al. 2015b, ApJL, 803, L21
Voit, G. M., Meece, G., Li, Y., et al. 2017a, ApJ, 845, 80
Voit, G. M., Meece, G., Li, Y., et al. 2017b, ApJ, 845, 80
Werner, N., Allen, S. W., & Simionescu, A. 2012, MNRAS, 425, 2731
Werner, N., Oonk, J. B. R., Sun, M., et al. 2014, MNRAS, 439, 2291
Yang, H.-Y. K., & Reynolds, C. S. 2016, ApJ, 818, 181
Young, L. M., Bureau, M., Davis, T. A., et al. 2011, MNRAS, 414, 940